12-2013

Micro-RVE modeling of mechanistic response in porous intermetallics subject to weak and moderate impact loading

A R. Nair
Rutgers State University

B A. Mason
Purdue University, bamason@purdue.edu

L J. Groven
Purdue University, lgroven@purdue.edu

S F. Son
Purdue University, sson@purdue.edu

A Strachan
Purdue University, Birck Nanotechnology Center, strachan@purdue.edu

See next page for additional authors

Nair, A R.; Mason, B A.; Groven, L J.; Son, S F.; Strachan, A; and Cuitino, A M., "Micro-RVE modeling of mechanistic response in porous intermetallics subject to weak and moderate impact loading" (2013). *Birck and NCN Publications.* Paper 1556.
http://dx.doi.org/10.1016/j.ijplas.2013.06.009

International Journal of Plasticity 51 (2013) 1–32

Contents lists available at SciVerse ScienceDirect

International Journal of Plasticity

journal homepage: www.elsevier.com/locate/ijplas

Micro-RVE modeling of mechanistic response in porous intermetallics subject to weak and moderate impact loading

A.R. Nair [a,*], B.A. Mason [b], L.J. Groven [b], S.F. Son [b], A. Strachan [c], A.M. Cuitiño [a]

[a] Department of Mechanical and Aerospace Engineering, Rutgers University, 98 Brett Road, Piscataway, NJ 08854, USA
[b] School of Mechanical Engineering, Purdue University, West Lafayette, IN 47907, USA
[c] School of Materials Engineering and Birck Nanotechnology Center, Purdue University, West Lafayette, IN 47907, USA

ARTICLE INFO

Article history:
Received 5 December 2012
Received in final revised form 28 June 2013
Available online 13 July 2013

Keywords:
Porous material
Heterogeneous material
Energetic material
Impact modeling
Finite elements

ABSTRACT

In this article we propose macroscopic (continuum) simulation schemes to predict response of porous heterogeneous material systems subjected to weak and moderate impact velocities. The proposed simulation model includes (1) an equation of state for porous solids that describes the evolution of porosity in the material as a function of shock pressure and, (2) a macroscopic rate dependent plasticity model for the porous composite that accounts for the deviatoric strength of the material at weak to moderate shock strengths. In addition, the numerical scheme employs cold-mixture theory to predict shock response of porous intermetallics. The material model is validated using gas-gun impact experiments on Ni/Al Intermolecular Reactive Composite (IRC) at 70% TMD. The proposed model is also used to understand the effect of microstructure on the material response predictions.

1. Introduction

Intermolecular Reactive Composites (IRCs) are a class of high energy density, structural materials that are capable of self-sustained exothermic reactions when subjected to thermal or mechanical initiation. A unique feature of these systems is the ability to undergo *gasless solid-state* reactions with little to no melting of the bulk material at threshold initiation energies (Reeves et al., 2010; Mukasyan et al., 2011; Manukyan et al., 2012). Due to this property, these materials are also called solid state reactive composites (SSRCs). Manukyan et al. (2012) observed that at impact velocities close to its threshold values (i.e., the minimum impact velocity required to initiate reactions), mechanically activated Ni/Al IRC powder compacts ignite through chemical reactions that occur on a time-scale much longer (on the order of milli-seconds) than the time required to mechanically equilibrate the material system (on the order of micro-seconds). While in recent years there has been a sustained effort to characterize these materials, there has been an evolving need to develop macroscopic models for energetic composites that are amenable to large scale computations. In this work, we propose a generalized continuum framework to model porous, heterogeneous materials that can be used to predict the deformed configuration and the localized stress-fields in the material as it undergoes impact assisted deformation. We envision that the proposed mechanistic model can be subsequently coupled with a suitable reaction model to predict initiation and propagation of chemistry in energetic materials. It has been noted that the distinct properties of porous IRCs are due to (a) spatial heterogeneity (i.e., multiple solid phases and pores) that helps localize energy through pore collapse and plastic deformation of grains to initiate reaction, and (b) an optimized material nano and microstructure with decreased inter-diffusional lengths that is key to sustaining reactions follow-

* Corresponding author.
E-mail addresses: abilash.nair@rutgers.edu, arnair@crimson.ua.edu (A.R. Nair).

0749-6419/$ - see front matter © 2013 Elsevier Ltd. All rights reserved.
http://dx.doi.org/10.1016/j.ijplas.2013.06.009

ing initiation. In the following paragraphs a review of the methods that has been proposed to model many facets of deformation in porous, heterogenous materials are discussed.

Mechanistically, porous materials are divergent in the manner in which shock energy is distributed and localized within the material relative to their dense (non-porous) counterparts. Porosity in the energetic material acts to localize shock energy into "hot-spots" within the bulk material that could induce a chemical reaction. In particular, shock compression in discrete particle systems undergo the following stages of densification as a function of increasing shock pressure (a) particle rearrangement (b) void collapse and particle deformation, and finally (c) bulk compression of the material system. Due to the complexities involved in modeling fine-scale physics of porous materials, computational schemes such as Eulerian hydrocodes (Benson et al., 1997; Eakins and Thadhani, 2007), discrete particle modeling and direct numerical simulation (Kumar et al., 1999; Barua et al., 2012) are popular choices in studying these materials. While these modeling techniques explicitly resolve the heterogeneities, common disadvantages include (a) the inability to study non-trivial boundary conditions and (b) the computational difficulty in scaling to larger system sizes and time-scales. The alternative is multi-scale modeling of these systems in a macroscopic setting in which the problem studied could be scaled to study longer time-scales (on the order of thermal equilibration of the system) and larger system sizes (on the order of sample sizes). However, the challenges involved in describing the physics of these materials in a macroscopic setting are significantly harder as discussed below.

Shock modeling of solids has been an active area of research since World War II. It has been noted that weak to moderate shock waves widely differ in behavior relative to strong shocks[1] (Germain and Lee, 1973; Wallace, 1980). At moderate shock strengths (i.e. at shock strengths lower than the dynamic yield strength of the material), the deviatoric strength of the solid plays an important part in shock response. It manifests as the classic elastic–plastic two wave structure in the shock response of ductile materials (Germain and Lee, 1973). However, wave propagation in discrete systems differ widely from their dense counterparts. Menikoff (2001) uses direct numerical simulation on powder beds subject to piston driven boundary conditions to study the influence of increasing shock strength on the mechanistic behavior of the powder bed. As expected, the material response at various shock strengths was observed to be strongly correlated to the discreteness of the material system. For weak shock strengths, material porosity does not decrease significantly behind the shock wave and the material system retains its discreteness which leads to attenuated shock waves with the transmitted waves being mostly dispersive.[2] In this phase, the material deforms largely due to particle rearrangement behind the compaction wave with sparse regions of the system beginning to interlock. For moderate input energies widespread particle interlocking leads to particle deformation which, depending on its character leads to material fracture and/or plastic deformation. In this regime, the material exhibits a stress bridging behavior along with a clearly defined two part elastic–plastic wave structure very similar to that in a fully dense material. Further increases in input energy result in a singular shock driven through the system in which dynamic compaction of the material occurs directly behind the shock wave. While it is intractable to include all features of the discrete system in a macroscopic continuum setting, it is still feasible to incorporate the effective behavior of the discrete system into the constitutive model with the choice of an appropriate equation of state (EOS).

Historically, the Mie-Gruneisen EOS (McQueen and Marsh, 1991; Meyers, 1994) has been extensively used to model shock response of solids. Simons and Legner (1982) derived a shock Hugoniot for porous solids in terms of cold pressure, cold energy and density of the porous material. The construction of the EOS follows the isochoric approach (McQueen and Marsh, 1991; Dijken and De Hosson, 1994), wherein the Gruneisen parameter is used to relate the deformation states in a dense solid (with a known pressure) to its porous counterpart (unknown pressure) to derive the shock EOS. The alternate choice to shock modeling in porous materials is the isobaric approach (Wu and Jing, 1996; Mostert and Viljoen, 1999) in which the specific enthalpy is used to derive the shock EOS in the porous solid. Dai et al. (2008) summarizes for nano-sized iron powder compacts either approach showed decreasing accuracy in predicting shock Hugoniot with increasing porosity. In general, either EOS is unable to predict shock Hugoniots for nano-sized powders with large porosities. In modeling multi-component mixtures, McQueen and Marsh (1991) proposed cold-mixture theories to determine shock pressure however in this approach the Gruneisen parameter is considered to be linearly dependent on specific volume, which may not true for all cases (Vocadlo et al., 2000). Zhang et al. (2011) derives shock EOS for porous intermetallic mixtures using a combination of the isobaric and isochoric approaches in addition to a non-linear relation between Gruneisen parameter and specific volume. Reding (2009) suggests as part of a multi-scale modeling strategy, two iterative techniques to determine shock pressure in multi-component porous energetic materials.

As discussed above, the discrete-system dynamics is characterized by its porosity at weak to moderate impact velocities. The empirical $p-\alpha$[3] model suggested by Herrmann (1969) is a widely used approach in compaction modeling of porous materials. The $p-\lambda$[4] model (Grady et al., 2000) is a generalization of $p-\alpha$ to treat mixtures with multiple-phases (such as void space filled with air/moisture). Micromechanics based RVE approaches have also been suggested to model pore collapse. Carroll and Holt (1972) derive static and dynamic pore collapse relations for an elastic-perfectly plastic spherical RVE model undergoing axi-symetric reduction in volume under the influence of an external pressure field. Tong and Ravichandran (1993) extended the Caroll and Holt model to study the effect of microinertia related to dynamic pore collapse in rate dependent viscoplastic

[1] In this paper, strong shocks refer to the pressure singularity that travels with velocity much larger than the bulk velocity of the solid material.
[2] It should be noted that in this scenario, the *shock* wave is primarily a dispersed pressure wave.
[3] α is the inverse solid volume fraction of the porous material.
[4] λ is the fraction of each phase in a multi-phase mixture.

matrix materials. More recently, Reding (2009) has extended the classical Caroll and Holt model to a twin sphere model to capture the effect associated with changes in mixture-morphology on pore collapse. An in-depth comparative study of the two methods have been reported in Fredenburg and Thadhani (2013).

As mentioned before, the purpose of this paper will be to provide a basis for large scale impact simulations of porous materials under the traditional finite element approach while still being able to resolve sub-grid physics (such as porosity) of the material. The primary advantage of such an approach will be the ability to simulate to larger time- and length scales and provide sample level prediction. It is envisioned that the developed method can be leveraged to predict and design multi-functional energetic materials. The generalized computational model in this work implements the approach outlined in Zhang et al. (2011) to predict the shock Hugoniot of any intermetallic mixture (with *no phase change*) in conjunction with the isochoric model proposed by Simons and Legner (1982) to determine the Hugoniot of the porous mixture. While, crystal plasticity models of intermetallic crystals (Cuitiño and Ortiz, 1993) do provide meso-scale description of plasticity that could be used in continuum simulations, we choose the rate dependent J_2 visco-plasticity model suggested in Cuitiño and Ortiz (1992), in the interest of tangible and inexpensive computations. In addition, the micromechanical model in Carroll and Holt (1972) is used to model pore-collapse in the material as a function of pressure. The proposed model will be validated using 1D simulation predictions against results from gas-gun experiments on Ni/Al binary IRCs. One-dimensional simulation validations of fully three dimensional constitutive models are not without precedent (e.g., Kuchnicki et al., 2008). It should be noted that the continuum formulation presented in this paper is generic in nature and in principle can be used to model any multi-material energetic composite. For the sake of completeness, we will also examine the effect of microstructure on material response predictions.

2. Constitutive model

In this section, the general framework for modeling material response of a porous heterogeneous material subjected to impact loading is outlined. At low input energies,[5] the shock strength is not large enough to cause widespread collapse of pores within the material. This results in dispersion of the loading wave due to wave reflections at material interfaces in addition to the internal reflections within individual particles that constitute the porous material. The proposed constitutive model must be representative of these events in a macroscopic setting. In classical shock theory for solids, the characteristic shock speed (U_s) versus particle velocity (u_p) curves are determined assuming that the material response is "hydrodynamic" in nature such that the shock pressure far exceeds the deviatoric strength of the material. The governing hydrodynamic equations in this scenario are as follows:

$$\rho_0 U_s = \rho(U_s - u_p), \quad p = p_0 + \rho_0 U_s u_p, \quad e - e_0 = \frac{1}{2}(p + p_0)(v_0 - v). \tag{1}$$

In general, the hydrodynamic assumption holds well for shock-pressures that exceed the Hugoniot elastic limit (HEL) of the material. However, a descriptive material model must account for the limiting behavior of the porous solid at weak to moderate shock strengths (Menikoff, 2001). The constitutive model considered in this work includes a porous shock EOS, rate dependent plasticity and pressure assisted void collapse model that accounts for the discrete particle behavior of the material in a macroscopic setting.

2.1. Porous equation of state

Porous mixtures[6] vary significantly in shock behavior with respect to their dense (non-porous) counterparts due to porosity and material inhomogeneity. In this work the porous equation of state is determined using the "isochoric" approach (similar to Simons and Legner, 1982) with the equations for cold pressure and energy approximated by the the Born–Meyer theory (Zharkov and Kalinin, 1971). The cold mixture theory suggested by Zhang et al. (2011) is used to predict the Hugoniot of the porous mixture. The basis of this approach follows from the Gruneisen approximation,

$$\left(\frac{\partial p}{\partial e}\right)_{v_s} = \frac{\gamma}{v_s}. \tag{2}$$

Shown in Fig. 1 is a graphical representation of the isochoric approach to relate the volume of the solid phase 'v_s' to the pressure 'p' of the porous solid. Using the definition of the Gruneisen parameter (Eq. 2) the Hugoniot for the dense (non-porous) material p_s can be determined as a function of the cold pressure 'p_c', cold energy 'e_c' of the system as follows (for details, Zhang et al., 2011),

$$p_s = \frac{v_s p_c - \gamma e_c}{v_s - \frac{\gamma}{2}(v_{s0} - v)}. \tag{3}$$

The equations for Born–Meyer cold (elastic) energy and pressure are (Zharkov and Kalinin, 1971),

[5] In impact scenarios, input energies correlate to impact velocities. Hence, a lower impact velocity implies a lower input energy.

[6] In this work, mixture refers to a solid of two or more constituents. Porous mixture on the other hand, refers to the multi-component material with voids.

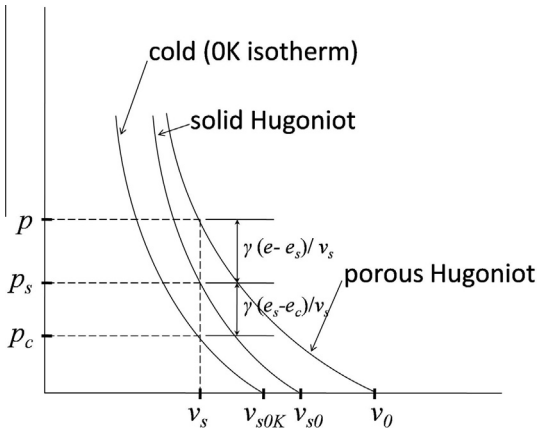

Fig. 1. Schematic to determine the porous Hugoniot from given cold curve and the Gruneisen parameters 'γ'. The Gruneisen approximation is used to relate the cold pressure p_c to the solid (fully dense) Hugoniot pressure p_s and finally to the pressure of the equivalent porous material.

$$e_c(v_s) = \frac{3Q}{\rho_{s0K}}\left\{\exp\left[q\left(1-\delta^{-1/3}\right)\right] - \delta^{1/3} - \frac{1}{q} + 1\right\}, \tag{4}$$

$$p_c(v_s) = \frac{de_c}{dv_s} = Q\delta^{2/3}\left\{\exp\left[q\left(1-\delta^{-1/3}\right)\right] - \delta^{2/3}\right\}. \tag{5}$$

where, 'Q' (units of pressure) and 'q' (non-dimensional) are parameters that describe the cold-energy curve. Compressibility δ is given as,

$$\delta = \frac{\rho_s}{\rho_{s0K}} = \frac{v_{s0K}}{v_s}. \tag{6}$$

Using this approach, the Gruneisen parameter (γ) is determined using the Dugdale–MacDonald relationship (McQueen and Marsh, 1991),

$$\gamma(v_s) = -\frac{v_s}{2}\frac{d^2\left(p_c v_s^{2/3}\right)/dv_s^2}{d\left(p_c v_s^{2/3}\right)/dv_s} - \frac{1}{3} = \frac{1}{6}\frac{q^2\delta^{-1/3}\exp\left[q\left(1-\delta^{-1/3}\right)\right] - 6\delta}{q\exp\left[q\left(1-\delta^{-1/3}\right)\right] - 2\delta}. \tag{7}$$

For intermetallics and other heterogenous materials, the cold energy and pressure is determined using mixture rules. For example, in a N component mixture (the mass fraction of each component being, m_i)

$$v_s = \sum_{i=1}^{N} m_i v_{si}, \tag{8}$$

$$e_c = \sum_{i=1}^{N} m_i e_{ci}(v_{si}), \tag{9}$$

$$\text{with,}\quad \sum_{i=1}^{N} m_i = 1. \tag{10}$$

For multi-component mixtures, the parameters 'Q' and 'q' in Eqs. (4) and (5) are determined using a non-linear curve fitting (such as Marquadt-Levenberg) of $e_c(v_s)$ (Eqs. (8)–(10)). Since the parameters required for the Born–Meyer equation are easily available (Zhang et al., 2011) the EOS proposed in this work has the added advantage of being able to predict shock characteristic for any multi-material SSRCs. The pressure in the porous solid then follows from Eq. (2) to arrive at the following relation (Dijken and De Hosson, 1994),

$$p(v_s) = \left[\frac{2v_s - \gamma(v_{s0} - v_s)}{2v_s - \gamma(v_0 - v_s)}\right]p_s(v_s) - \frac{2\gamma(e_0 - e_{s0})}{\gamma(v_0 - v_s) - 2v_s}. \tag{11}$$

where, v_{s0} is the *initial* specific volume of the solid material, v_0 is the specific volume of the porous mixture, e_0 is the initial specific energy of the porous mixture, and e_{s0} is the initial specific energy of the solid mixture. Assuming, $e_0 \approx e_{s0}$ (i.e. assuming that the initial energies of the dense and porous materials are same) and substituting Eq. (3) in Eq. (11) we get,

$$p(v_s) = \frac{2(v_s p_c - \gamma e_c)}{2v_s - \gamma(v_0 - v_s)}. \tag{12}$$

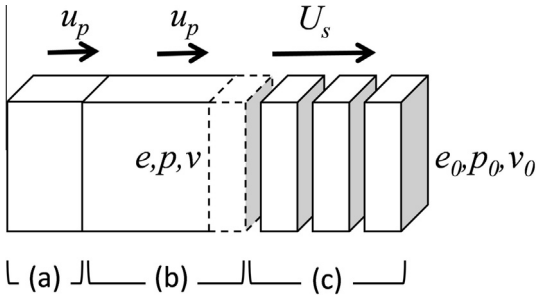

Fig. 2. Schematic showing the various zones of the consolidation process in shocked powder materials (from, Dijken and De Hosson, 1994). Zone (a) is fully consolidated material moving with material velocity u_p, Zone (b) is the process zone where shock assisted pore collapse occurs (velocity of shock front is U_s) and Zone (c) is un-collapsed region of the powder material. The powder is assumed to be separate solid plates collapsing sequentially on the shock-wave front.

Hence we have the constitutive relationship that relates the level of solid phase deformation v_s to the pressure generated. In other words, if we define a quantity α as the inverse solid volume fraction (or distension) of the solid, then $p(v_s) \equiv p(v/\alpha)$. Temperature hikes due to shock assisted heating 'ΔT^S' can be calculated from the following ordinary differential equation (see e.g. McQueen and Marsh, 1991),

$$\frac{dT^S}{dv_s} = -T\frac{\gamma}{v_s} + \frac{1}{2C_v}\left[(v_{s0} - v_s)\frac{dp}{dv_s} + p\right]. \tag{13}$$

It should be noted that the proposed equation of state (EOS) model inherently assumes that the shock pressure is large enough to collapse and consolidate the powder material as the shock wave passes through it (see Fig. 2). However, for weak to moderate shock strengths the material rigidity and resistance to void collapse is significant and needs to be accounted for accurately. A material model for pore collapse is discussed in Section 2.3. It should be noted that the computational model can be used with other models for shock pressure such as the "isobaric" approach (see, Wu and Jing, 1996).

2.2. Rate dependent plasticity

Impact simulations of ductile materials must account for rate-dependency in the material due to the typically large loading strain-rates (see e.g., Brünig and Driemeier, 2007). Recent work in the field of plasticity modeling at intermediate to high strain rates have addressed topics such as surface texture evolution as a function of strain-rate and ambient temperature (Pandey et al., 2013) and damage evolution (Shojaei et al., 2013) in polycrystalline materials. Finely tuned crystal plasticity models have also been proposed to accurately model the dynamic response of materials in the large strain rate regimes (Austin and McDowell, 2012). However, in the interest of expediting computations with a lower overhead we adopt a simple rate-dependent J_2 visco-plasticity approach (Cuitiño and Ortiz, 1992) that is used to model the deviatoric response of the material. Material properties for the rate-dependent plasticity model are determined by homogenizing the porous RVE to find effective properties of the bulk material (Fig. 3). The material bulk modulus (K) and shear modulus (μ) are estimated as a function of material porosity (φ) using the following relations (Ramakrishnan and Arunachalam, 1990),

$$K(\varphi) = K_s(1-\varphi)^2/(1+b_k\varphi), \tag{14}$$

$$\mu(\varphi) = \mu_s(1-\varphi)^2/(1+b_g\varphi), \tag{15}$$

$$\text{where, } b_k = (1+v_s)/[2(1-2v_s)] \text{ and } b_g = (11-19v_s)/[4(1+v_s)], \text{with } \varphi = 1 - \frac{v_s}{v}.$$

The parameters v_s, K_s and μ_s are material properties of the isotropic solid-phase (non-porous) material. For intermetallics, these material properties can be determined using a simple rule-of-mixtures. The above equations provide a conservative estimate of the material properties as the porosity of the material is increased. The initial yield stress of the porous composite material σ_0 can be determined independently (e.g. see Section 4) if not known a priori. From finite-deformation kinematics, the deformation can be decomposed multiplicatively into isochoric plastic deformation $\mathbf{F}^p$ ($\det(\mathbf{F}^p) = 1$) and pure elastic deformation $\mathbf{F}^e$,

$$\mathbf{F} = \mathbf{F}^e\mathbf{F}^p. \tag{16}$$

The plastic deformation is assumed to follow the Prandtl–Reuss flow rule,

$$\dot{\mathbf{F}}^p\mathbf{F}^{p-1} = \dot{\epsilon}^p\frac{3\mathbf{s}^e}{2\sigma}, \tag{17}$$

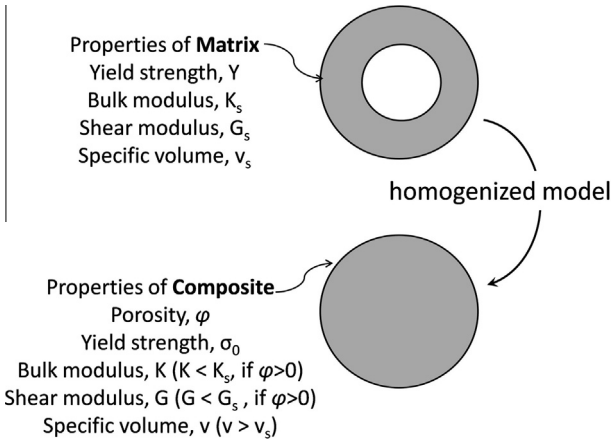

Fig. 3. Nomenclature of homogenized material of the porous material.

where, ϵ^p is the effective plastic-strain, $\mathbf{s}^e = \frac{\mu}{2}\text{dev}[\log \mathbf{C}^e]$ is the stress-deviator of the IInd Piola–Kirchoff stress tensor, $\mathbf{C}^e = \mathbf{F}^{eT}\mathbf{F}^e$ is the elastic right Cauchy–Green tensor, and $\sigma = \sqrt{(3/2)\mathbf{s}^e : \mathbf{s}^e}$ with, $\text{dev}[\cdot] = [\cdot] - \frac{1}{3}\text{tr}[\cdot]\mathbf{I}$, $\mathbf{I}$ is the identity tensor. The following assumptions are made on the hardening behavior of the material in-order to solve Eq. (17),

$$\sigma = g\left(\frac{\dot{\epsilon}^p}{\dot{\epsilon}_0^p} + 1\right)^{\frac{1}{m}}, \tag{18}$$

$$g = \sigma_0\left(\frac{\epsilon^p}{\epsilon_0^p} + 1\right)^{\frac{1}{n}}, \tag{19}$$

where, g is the flow-stress, σ_0 is the initial yield stress, ϵ_0^p and $\dot{\epsilon}_0^p$ are the values of reference strain and reference strain-rates, respectively while m and n are rate-sensitivity and strain-hardening exponents, respectively. In shock simulations, of particular interest is to quantify the amount plastic work and the temperature excursions that occur as a result of plastic dissipation in the body. Assuming that all plastic work is converted to increase in temperature we arrive at the following relation,

$$\Delta T^p = \frac{1}{c_p}\int_0^t g(\epsilon^p)\,\dot{\epsilon}^p dt'. \tag{20}$$

2.3. Micro RVE model for porosity

In this work, porosity (φ) is an internal state variable that varies as a direct function of the applied pressure in the material. The classic Caroll and Holt RVE model (Carroll and Holt, 1972) describes pore collapse in the material as a function of shock pressure. Shown in Fig. 4 is a detailed schematic explaining the setup of the continuum model with porosity, with a_0 and b_0 being geometry parameters related to the characteristic pore size of the system (Carroll and Holt, 1972). Before we proceed we introduce the following nomenclatures,

$$\alpha_0 = \frac{100}{\rho_{00}} = \frac{v_0}{v_{s0}} = \frac{\rho_{s0}}{\rho_0}, \tag{21}$$

$$\phi_0 = 1 - \frac{1}{\alpha_0}, \tag{22}$$

where, α is the solid distension or inverse solid volume fraction, $\rho_s\ (= 1/v_s)$ is initial density of the solid-phase material, $\rho\ (= 1/v)$ is reduced density of the porous material, and ρ_{00} is the targeted mean density (TMD) of the porous material (such that if, ρ_{00}=70% then porosity $\varphi = 0.3$ and $\alpha = 1.428$). The subscript '0' refers to variables defined at zero applied stress (or stress free state of the material). From Carroll and Holt (1972) the solid distension of a spherical shell undergoing static pore collapse as a function of shock pressure is derived to be,

$$p = \begin{cases} \frac{4\mu_s(\alpha_0-\alpha)}{3\alpha(\alpha-1)} & \text{if } \alpha_0 \geqslant \alpha \geqslant \alpha_1, \\ \frac{2}{3}Y\left\{1 - \frac{2\mu_s(\alpha_0-\alpha)}{Y\alpha} + \ln\left[\frac{2\mu_s(\alpha_0-\alpha)}{Y(\alpha-1)}\right]\right\} & \text{if } \alpha_1 \geqslant \alpha \geqslant \alpha_2, \\ \frac{2}{3}Y\ln\frac{\alpha}{\alpha-1} & \text{if } \alpha_2 \geqslant \alpha \geqslant 1, \end{cases} \tag{23}$$

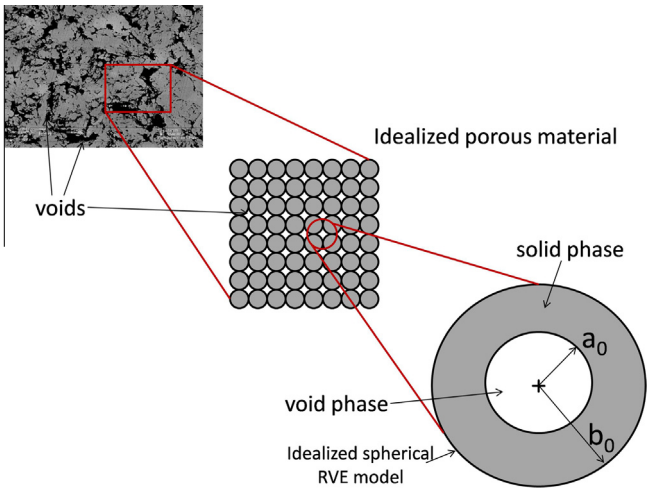

Fig. 4. Schematic showing the idealization of the microstructure to the spherical RVE model in Carroll and Holt (1972) with a_0 and b_0 as the inner and outter radii of the the spherical model, which are related to the size of the voids (pores).

where, Y is the yield stress of the matrix material, α_1 and α_2 are porosity measures at elastic/elastic–plastic and the elastic–plastic/plastic transition phases, respectively of spherical shell deformation given as,

$$\alpha_1 = \frac{2\mu_s\alpha_0 + Y}{2\mu_s + Y}, \tag{24}$$

$$\alpha_2 = \frac{2\mu_s\alpha_0}{2\mu_s + Y}. \tag{25}$$

It should be noted that the static pore collapse relations (Eq. 23) are independent of the characteristic pore size of the system. In an attempt to further simplify calculations we ignore the transitional modes of deformation (viz. $\alpha_1 \geqslant \alpha \geqslant \alpha_2$) such that Eq. (23) can be inverted to determine material distension 'α' (where, $\alpha^{-1} = 1 - \varphi$) as follows,

$$\alpha = \begin{cases} \alpha_0 & \text{if } p \leqslant p_{\text{crit}}, \\ [1 - \exp(-3p/2Y)]^{-1} & \text{otherwise}, \end{cases} \tag{26}$$

with,

$$p_{\text{crit}} = \frac{2}{3} Y \ln \frac{\alpha_0}{\alpha_0 - 1}. \tag{27}$$

Hence, it is implicitly assumed that the spherical shell does not yield until the pressure exceeds the critical value of p_{crit}. This assumption remains true in general whenever, $Y \ll (2\mu_s + Y)$, since α does not change appreciably in this scenario. However, as discussed in Section 2.3.1, the assumption introduces some spurious numerical behaviors. A more complete discussion on the equations are available in Carroll and Holt (1972). In Section 3.3 numerical implementation of the above equations in an explicit update of the state variables is discussed in detail.

2.3.1. Implications of critical pressure (p_{crit})

Using the jump conditions listed in Eq. (1) the following relations for particle velocity (u_p) and shock speed (U_s) in terms of shock pressure (p) and current specific volume (v) of the porous solid can be derived for one-dimensional shock flows,[7]

$$u_p = \sqrt{p(v_0 - v)}, \tag{28}$$

$$U_s = v_0 \sqrt{\frac{p}{v_0 - v}}. \tag{29}$$

Fig. 5 is a plot of shock velocity (Eq. 29) versus particle velocity (Eq. 28) for the Al-2024 system (experimental data from, Marsh (1980)). The plot compares results from two approaches namely, the isochoric approach (Eq. 12) and and the isobaric approach (Wu and Jing, 1996). The numerical values for the parameters in Eq. (4) are chosen from Zhang et al. (2011) with $\alpha_0 = 1.68$ (for 59.7 % TMD) and $\alpha_0 = 1.25$ (for 79.9 % TMD). As can be seen clearly, as $u_p \to 0, U_s$ tends to unrealistically large

[7] assuming p_0 is small relative to p.

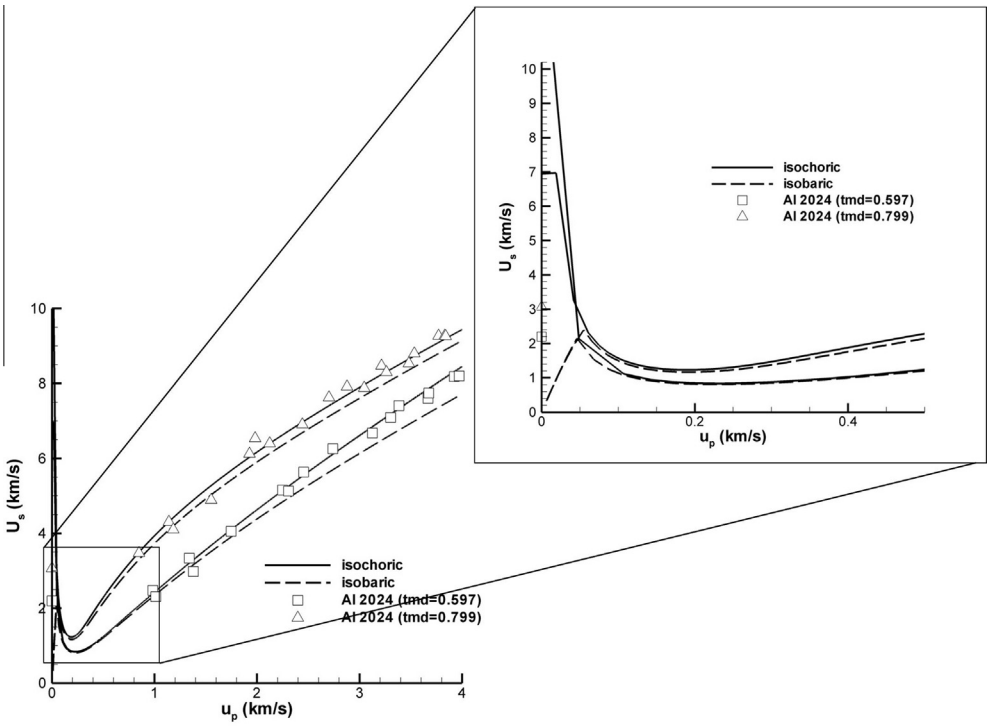

Fig. 5. Schematic of anomalous behavior $U_s - u_p$ predicted by isochoric (this work), isobaric (Wu and Jing, 1996) compared to experimental data for 59.7 and 79.9% TMD Al-2024 (Marsh, 1980).

numbers. The numerical abnormality occurs as a direct result of the non-physical restriction on α as long as $p < p_{\text{crit}}$. In order to resolve this numerical behavior, we propose the following simple fix: Compute and iteratively determine the value of $v = v^*$ at which $dU_s/du_p = 0$. Then for all deformation levels that satisfy, $v^* < v \leqslant v_0$, the pressure is calculated as,

$$p = p^*\left(\frac{1-J}{1-J^*}\right), \tag{30}$$

where, p^* is the pressure corresponding to deformation v^* (i.e., $p^* \equiv p(v^*/\alpha^*)$ in Eq. (12), while $J = v/v_0$ and $J^* = v^*/v_0$. With this fix, the anomalous behavior is eliminated as shown in Fig. 6. It should also be noted that with this fix the bulk wave speed is bounded and not allowed to attain unreasonable values.

2.3.2. An alternate RVE model

The spherical void collapse model is a widely used micro-mechanical model to relate macroscale mechanics to microscale events such as pore collapse and void closures in porous materials when subjected to pressure ingresses. In this section, we propose an alternate RVE model to the classic and oft-used Carroll and Holt model. Specifically, we seek to incorporate similarity solutions (Hill et al., 1989), characterized through particle mechanics algorithms (Gonzalez and Cuitiño, 2012) into the macroscale continuum simulations discussed in this work. In this work, the microstructure is assumed to have a body centered cubic (BCC) packing (68.02% TMD), is quasi-statically subjected to hydrostatic compression (see, Fig. 7). The pressure developed inside the packing is then determined as a function of solid distension (α) which can be used to inform the macroscale models developed in Section 2. However, it is difficult to determine the volume change associated with the solid phase deformations in particle level simulations. Hence, for the purposes of this paper, α is determined as v/v_{s0}, wherein v is the current (deformed) volume of the porous solid under hydrostatic compression.

The similarity solution (Hill et al., 1989) assumes a material with the following constitutive relation,

$$\sigma = \kappa\epsilon^{1/m}, \tag{31}$$

where, σ is stress, κ is material constant, $1/m$ is a hardening parameter and ϵ is a strain measure in a particle–particle interaction (Gonzalez and Cuitiño, 2012). Thus, the force–deformation relationship at the particle level is modeled by the following scaling function,

$$F \propto \kappa\left(\frac{\gamma_p}{D}\right)^{1+\frac{1}{2m}}, \tag{32}$$

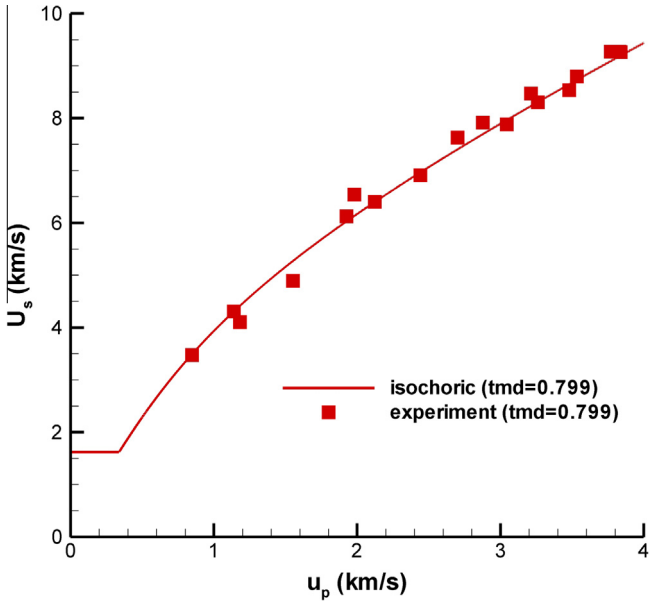

Fig. 6. Corrected $U_s - u_p$ behavior predicted by isochoric (this work) compared to experimental data for 79.9% TMD Al-2024 (Marsh, 1980).

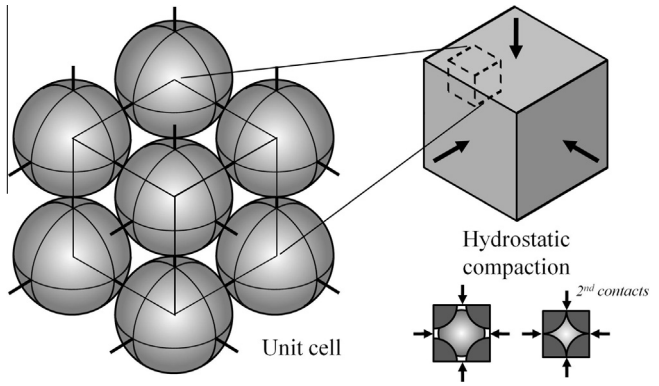

Fig. 7. Schematic of micro-scale packing of particles in a Body Centered Cubic (BCC) setting. Picture courtesy: Gonzalez and Cuitiño (2012).

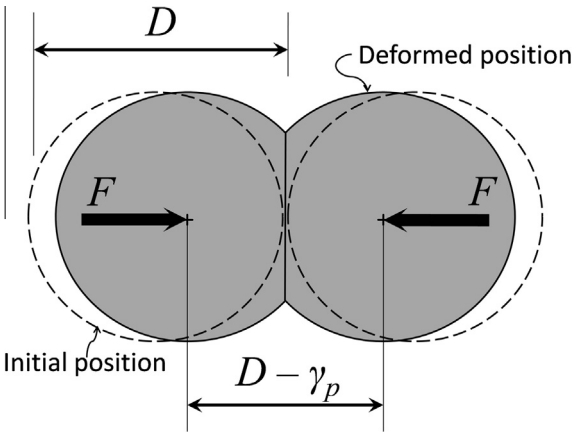

Fig. 8. Schematic of two-body particle interaction as a function of material overlap γ_p.

where, F is the inter-particle force and γ_p/D is a deformation measure (Gonzalez and Cuitiño, 2012) with D the diameter of the particle and γ_p is the overlap of the particles (see, Fig. 8). Eq. 32 is parametrized by curve-fitting to the following hardening law,

$$\sigma = Y\left(1+\frac{\epsilon}{\epsilon_0}\right)^{1/n}, \tag{33}$$

where, the parameters in Eq. (33) carry the same meaning as in Section 2.2. When parameters in Eq. (31) are determined (see, Section 5.1), detailed particle level simulations can be used to determine an equation of state that can be directly used in macroscopic simulations. In Section 5.1, the effect of RVE choice on the macroscopic simulation predictions are discussed in detail. Specifics on the implementation of microscopic RVE model are also included.

3. Numerical implementation

In this section we discuss the details to implementing the constitutive model introduced in Section 2 within a traditional Finite Element Analysis (FEA) approach. As previously indicated, the current formulation primarily focuses on the mechanistic response of the (porous) energetic material subject to threshold impact loading. Mechanically activated binary Ni/Al IRC specimens were observed to chemically react long after the system reached full-mechanical equilibration (Reeves et al., 2010; Manukyan et al., 2012). Furthermore, IRCs undergo gas-less reactions in the solid phase when subjected to threshold impact velocities. This allows us to decouple any mechano-chemical phenomena and focus on the deformation characteristics of porous IRCs during its period of mechanical equilibration at threshold impact loadings. Hence, we adopt the conventional Lagrangian formulation of solid mechanics for our analysis (Section 3.1). In Section 3.3, algorithms are suggested that could be used to incorporate the micro-RVE compaction models into the macroscopic analysis setting. Also discussed is the manner in which shock assisted heating is computed during the constitutive update.

3.1. Lagrangian equations of motion

Suppose that a material body in its initial configuration B_0 at initial time t_0 deforms to configuration B at time 't'. We define a vector function $\boldsymbol{\varphi}(\mathbf{X},t)$, that maps a material point located at $\mathbf{X}$ to a point $\mathbf{x}$ in the deformed configuration such that,

$$\mathbf{x} = \boldsymbol{\varphi}(\mathbf{X},t) \quad \forall \mathbf{X} \in B_0. \tag{34}$$

The material deformation can be described with recourse to the deformation gradient $\mathbf{F}(\mathbf{X},t)$ defined as,

$$\mathbf{F} = \nabla_0 \boldsymbol{\varphi} \quad \forall \mathbf{X} \in B_0, \tag{35}$$

where, ∇_0 is the gradient operator in the reference (material) frame $\left(\nabla_0 \equiv \frac{\partial}{\partial \mathbf{X}}\right)$. In the Lagrangian setting, strong forms of the conservation of mass and linear-momentum for any material point $\mathbf{X} \in B_0$ are stated as follows,

$$\dot{\rho_0} = 0 \quad \forall \mathbf{X} \in B_0, \tag{36}$$

$$\rho_0 \ddot{\boldsymbol{\varphi}} = \nabla_0 \cdot \mathbf{P} + \mathbf{B} \quad \forall \mathbf{X} \in B_0, \tag{37}$$

where, $\mathbf{P}(\mathbf{X},t)$ is the first Piola–Kirchoff stress tensor, $\mathbf{B}(\mathbf{X},t)$ is the body force per unit mass and $\rho_0(\mathbf{X})$ is the initial density of the material. Material velocity and accelerations can be determined by taking appropriate time derivatives of the function $\boldsymbol{\varphi}$. The boundary and traction conditions on the bounding surfaces of the body are,

$$\boldsymbol{\varphi} = \overline{\boldsymbol{\varphi}}, \quad \forall \mathbf{X} \in \partial B_{0u}, \tag{38}$$

$$\mathbf{P} \cdot \mathbf{N} = \overline{\mathbf{T}}, \quad \forall \mathbf{X} \in \partial B_{0T}, \tag{39}$$

where, $\overline{\boldsymbol{\varphi}}(\mathbf{X},t)$ is the specified displacement on surface ∂B_{0u} and $\overline{\mathbf{T}}(\mathbf{X},t)$ is the applied traction on surface ∂B_{0T}. The traction and displacement surfaces jointly subscribe to $\partial B_{0u} \cup \partial B_{0T} = \partial B_0$ and $\partial B_{0u} \cap \partial B_{0T} = \phi$, where ∂B_0 is the bounding surface of the volume B_0. The Cauchy stress ($\boldsymbol{\sigma}$) has the following additive structure,

$$\boldsymbol{\sigma} = \boldsymbol{\sigma}^e + \boldsymbol{\sigma}^v, \tag{40}$$

where, $\boldsymbol{\sigma}^e$ is the stress tensor resulting from material constitutive relations and $\boldsymbol{\sigma}^v$ is the viscous stress added to the constitutive model in shock simulations to ameliorate numerical ringing. Following an assumption of material isotropy the constitutive model for shock response is written as a sum of a bulk pressure p and the deviatoric response of the system that follows from the plastic deformation model described in the previous sections,

$$\boldsymbol{\sigma}^e = -p\mathbf{I} + \frac{1}{J}\mathbf{F}^e \mathbf{s}^e \mathbf{F}^{eT}. \tag{41}$$

In numerical simulations of shock, it is convenient to add viscous stresses in lieu of numerical instability that occurs due to the sudden change in field variables across the shock front. Following Lew et al. (2001) we choose the viscous stresses to have the following format,

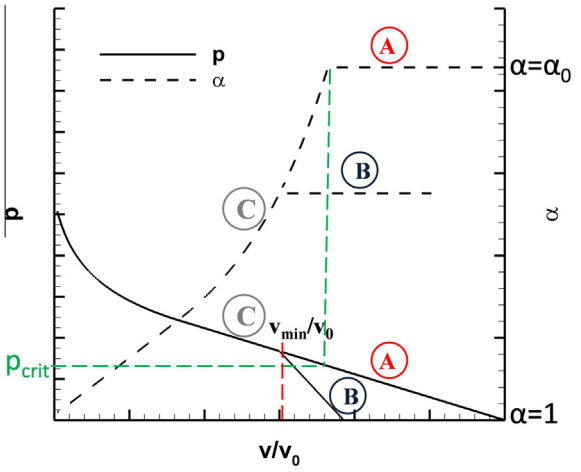

Fig. 9. Schematic for variation of α as a function of pressure p. Zone (A) loads the material continuously beyond $p > p_{crit}$, Zone (B) is unloading the material in which α remains constant, while in Zone (C) shows the loading path until full pore-collapse in the material.

$$\boldsymbol{\sigma}^{v} = 2\eta\,\mathrm{dev}\left[\mathrm{sym}(\dot{\mathbf{F}}\mathbf{F}^{-1})\right], \tag{42}$$

where, η is the viscosity of the material and sym$[\cdot]$ denotes the symmetric part of the tensor. Finally, to convert between Cauchy stress tensor $\boldsymbol{\sigma}$ and the Ist Piola-Kirchoff (in Eq. (37)) we use the following identity,

$$\mathbf{P} = J\boldsymbol{\sigma}\mathbf{F}^{-T}. \tag{43}$$

3.2. Temporal discretization

The governing equation in Eq. (37), can be discretized in time using the Newmark time-stepping algorithm. The displacement, velocity and acceleration update at time 'n' (t_n) for the generalized Newmark update is given by,

$$\boldsymbol{\varphi}_{n+1} = \boldsymbol{\varphi}_n + \Delta t\dot{\boldsymbol{\varphi}}_n + \Delta t^2[(1/2-\beta)\ddot{\boldsymbol{\varphi}}_n + \beta\boldsymbol{\varphi}_{n+1}], \tag{44}$$

$$\dot{\boldsymbol{\varphi}}_{n+1} = \dot{\boldsymbol{\varphi}}_n + \Delta t[(1-\gamma)\ddot{\boldsymbol{\varphi}}_n + \gamma\boldsymbol{\varphi}_{n+1}], \tag{45}$$

$$\rho_0\ddot{\boldsymbol{\varphi}}_{n+1} = \nabla_0\cdot\mathbf{P}_{n+1} + \mathbf{B}_{n+1}, \tag{46}$$

where, β and γ are Newmark's parameters that are chosen to be 0 and $\frac{1}{2}$, respectively, in accordance with an explicit time-stepping strategy, Δt is the time-step and the subscript 'n' refers to quantities at time t_n. Eq. (36) is trivially satisfied since, $\rho_0 \equiv \rho_0(\mathbf{X})$. The updated stresses follow from Eqs. (40) and (43) as,

$$\mathbf{P}_{n+1} = \mathbf{P}^{e}_{n+1} + \mathbf{P}^{v}_{n+1}, \tag{47}$$

where,

$$\mathbf{P}^{e}_{n+1} = J_{n+1}\boldsymbol{\sigma}^{e}_{n+1}\mathbf{F}^{-T}_{n+1}, \tag{48}$$

$$\mathbf{P}^{v}_{n+1} = J_{n+1}\boldsymbol{\sigma}^{v}_{n+1}\mathbf{F}^{-T}_{n+1}. \tag{49}$$

The quantities $\boldsymbol{\sigma}^{e}_{n+1}$ and $\boldsymbol{\sigma}^{v}_{n+1}$ are determined using Eqs. (41) and (42). The specific form of the incremental stresses and their evaluations are described in detail in the following section. Viscous stresses are computed using a finite difference approximation for $\dot{\mathbf{F}}_{n+1}$ (Radovitzky and Ortiz, 1999).

3.3. Incremental equations

The implementation of the constitutive models discussed in Section 2 follow a non-trivial update during the course of time-integration. In particular, the thermodynamic update of the system (specifically, EOS pressure and temperature) and update of system porosity are computations central to the simulation of energetic material. For discussions on plasticity update the readers is suggested to refer to Cuitiño and Ortiz (1992) for details.

3.3.1. Update of system porosity

Shown in Fig. 9 is a schematic description of the porosity model discussed in Section 2.3. It depicts in detail the volumetric compression of the porous material as it is quasi-statically loaded (to partial densfication), unloaded and subsequently loaded until complete compaction ($\alpha = 1$). As shown in the figure, in Zone (A) the material is loaded to above p_{crit}, at which point the α parameter begins to decrease (see, Eq. (26)). In Zone (B) the material is relaxed from a state of incomplete compaction ($\alpha > 1$). We indicate this release point with $v = v_{\min}$. The material unloads along a straight line path with α = constant. Subsequent loading in Zone (C) loads the system to higher pressures during which the system retraces the straight-line path (with constant porosity) until volume deformation reduces to below $v_{\min}$. As $v < v_{\min}$, the material rejoins the Hugoniot curve derived in Eq. (12). For the sake of convenience, we will denote $J_p = v_{\min}/v_0$, which physically represents the amount of plastic (irrecoverable) volume reduction due to the consolidation process. We will define two additional quantities, p_{un} as the pressure on the Hugoniot curve at $J = J_p$, and J_{un}, as the volume deformation of the porous solid at which $p = 0$ while unloading. Hence, the equation of the straight line for all deformations that satisfy $J_p < J < J_{\text{un}}$ are given as,

$$p(J) = p_{\text{un}}\left(\frac{J - J_{\text{un}}}{J_p - J_{\text{un}}}\right). \tag{50}$$

Algorithm 1. Calculate p_{n+1} and α_{n+1} for Static Pore Collapse

Require: $J_{n+1} > 0$ and $J_{n+1} < 1$ as material is loaded
1: **if** $J_{n+1} < J_p$ **then**
2: **if** $\alpha_n > 1$ **then**
3: Determine solid volume $v_{s,n+1}$, by minimizing the residual $f(v_s, \alpha) = \alpha v_s - J v_0$ through non-linear iteration
4: **else**
5: Compute solid deformation, $v_{s,n+1} = J_{n+1} v_0$
6: **end if**
7: Compute $p_{n+1} \equiv p_{n+1}(v_{s,n+1})$ using Eq. (12) or Eq. (30)
8: Update α_{n+1} using Eq. (26)
9: Update K, μ using Eqs. (14) and (15), respectively
10: Store $p_{\text{un}} = p_{n+1}, J_{\text{un}} = \frac{\alpha_{n+1}}{\alpha_0}$ and $J_p = J_{n+1}$
11: **else**
12: **if** $J_{n+1} \leqslant J_{\text{un}}$ **then**
13: $p_{n+1} = p_{\text{un}}\left(\frac{J_{n+1} - J_{\text{un}}}{J_p - J_{\text{un}}}\right)$
14: **end if**
15: **end if**

A detailed update of the porosity state variable is given in Algorithm 1. In determining the deformed solid specific volume in compression the residual function $f(v_s, \alpha) = \alpha v_s - J v_0$ needs to be minimized where, α is computed from Eq. (26) with the pressure given by $p \equiv p(v_s)$ using Eqs. (12) or (30). Since, the Newton–Raphson method is particularly vulnerable in slipping to numerical pitfalls during the minimization procedure, it is recommended that the bisection scheme be used to minimize the residual. If at any step 'n', should the material unload (i.e., $J_{n+1} > 1$), then the porosity (or α remains constant) and the solid volume and pressure update is simply given by the following equations,

$$v_{s,n+1} = v_{s,n}\frac{J_{n+1}}{J_n}, \tag{51}$$

$$p_{n+1} = K\left(\frac{\alpha_0}{J_{n+1}\alpha_n} - 1\right). \tag{52}$$

3.3.2. Update of system temperature due to shock heating and plastic dissipation

The incremental forms of Eqs. (13) and (20) are used to determine the shock assisted heating of the proposed continuum model for energetic materials. The heat update is the singularly most important update that couples the mechanistic response of the material to the generation of thermal hot-spots in the material that could potentially result in run away chemical reactions in the simulation of energetic materials. The plastic heat update is performed through a trapezium integration approach in time as follows,

$$\Delta T^{\text{p}}_{n+1} = \Delta T^{\text{p}}_n + \left(\frac{g(\epsilon^p_{n+1}) + g(\epsilon^p_n)}{2}\right)\frac{\dot{\epsilon}^p_{n+1}}{C_p}\Delta t, \tag{53}$$

where, the flow stress (g) is updated using Eq. (18), while the current plastic-hardening rate ($\dot{\epsilon}^p_{n+1}$) and plastic strain (ϵ^p_{n+1}) are computed using techniques discussed in Cuitiño and Ortiz (1992). The incremental equations for calculating temperature due to shock heating are,

$$\delta T^S_{n+1} = \left.\frac{dT}{dv_s}\right|_{n+1} (v_{s,n+1} - v_{s,\min}), \tag{54}$$

where, $v_{s,\min}$ is the minimum value of solid deformation in the loading history of the porous material, while $\left.\frac{dT}{dv_s}\right|_{n+1}$ can be computed from Eq. (13) such that,

$$\left.\frac{dT}{dv_s}\right|_{n+1} = -T^n \frac{\gamma_{n+1}}{v_{s,n+1}} + \frac{1}{C_v}\left[(v_{s0} - v_{s,n+1})\left.\frac{dp}{dv_s}\right|_{n+1} + \frac{p_{n+1}}{2}\right], \tag{55}$$

where

$$\left.\frac{dp}{dv_s}\right|_{n+1} = \frac{2\left[(1+\gamma_{n+1})p_{c,n+1} + v_{s,n+1}\left.\frac{dp_c}{dv_s}\right|_{n+1} - e_{c,n+1}\left.\frac{d\gamma}{dv_s}\right|_{n+1}\right] - p_{n+1}\left[2 + \gamma_{n+1} + (v_{s,n+1} - v_0)\left.\frac{d\gamma}{dv_s}\right|_{n+1}\right]}{2v_{s,n+1} - \gamma_{n+1}(v_0 - v_{s,n+1})}, \tag{56}$$

$$\left.\frac{dp_c}{dv_s}\right|_{n+1} = -\frac{Q\delta^{5/3}_{n+1}}{3v_{s0}}\left\{(q\delta^{-1/3}_{n+1} + 2)\exp\left[q\left(1 - \delta^{-1/3}_{n+1}\right)\right] - 4\delta^{2/3}_{n+1}\right\}, \tag{57}$$

$$\left.\frac{d\gamma}{dv_s}\right|_{n+1} = \frac{-\delta^2_{n+1}}{v_{s0}}\left\{\frac{36\gamma_{n+1} - 18 - q^2\delta^{4/3}_{n+1}(1 + 6\gamma_{n+1} - q\delta^{-1/3})\exp\left[q\left(1 - \delta^{-1/3}_{n+1}\right)\right]}{18q\exp\left[q\left(1 - \delta^{-1/3}_{n+1}\right)\right] - 36\gamma_{n+1}}\right\}. \tag{58}$$

The compressibility is computed as $\delta_{n+1} = v_{s0K}/v_{s,n+1}$. It should be noted that the summation is computed only when $v_{s,n+1} < v_{s,\min}$. Hence, total temperature rise from shock is,

$$\Delta T^S_{n+1} = \Delta T^S_n + \delta T^S_{n+1}. \tag{59}$$

4. Results

The predictions from the proposed continuum model were tested using results from gas-gun shear impact experiments on Ni/Al binary IRC in a 30/70 mass fraction with 70% initial TMD (ρ_{00}). A detailed description on material processing and thermal characterization of Ni/Al IRCs are available in Reeves et al. (2010). The experimental setup is shown in Fig. 10. Fig. 11 is a schematic of the one-dimensional simulation setup to validate the proposed constitutive model. A projectile, accelerated through a gas gun, impacts the back of a steel plunger (which has a flat geometry) with a chosen velocity. The kinetic energy of impact is absorbed as deformational energies first within the steel plunger and subsequently by the compact specimen. The experimental setup is instrumented to study the deformation behavior of the specimen during the pressurization process. Fig. 12 is a schematic of the setup to study material deformation in a compact specimen subjected to impact with a flat plunger. As shown in the figure, the surface of the compact specimen is demarcated with straight lines

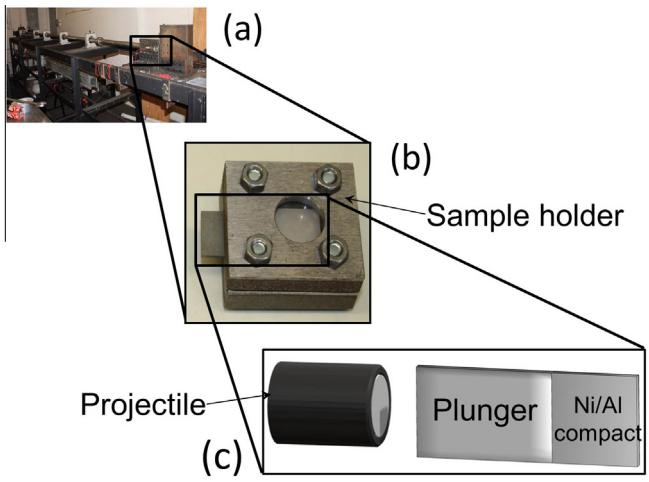

Fig. 10. Experimental setup of (a) gas-gun experiments on Ni/Al (30/70) in Purdue Materials Laboratory, (b) Sample holder with circular window containing specimen-plunger assembly, and (c) cut away showing configuration of impact specimen setup inside gas-gun assembly.

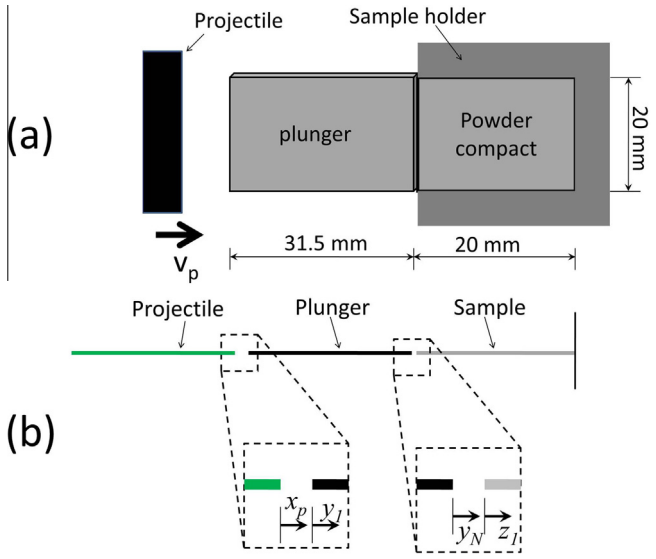

Fig. 11. Schematic of simulation setup. Shown in (a) is the dimensions of powder compact sample and *flat* steel plunger. Also indicated is the direction of projectile propagation with velocity 'v_p' before impact with plunger (b) is the equivalent 1D model with the displacements of contact points between three bodies indicated.

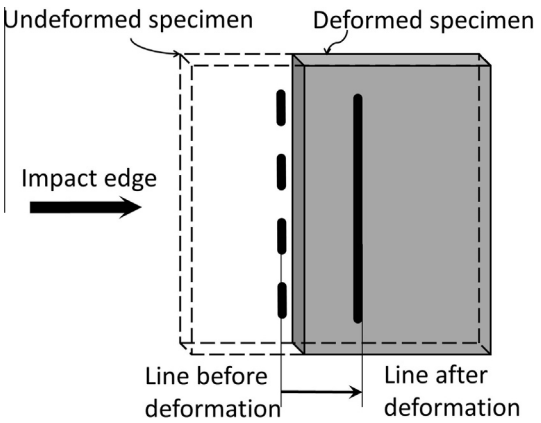

Fig. 12. Schematic of experimental setup to to track material deformation inside the compact specimen during the dynamic compaction process.

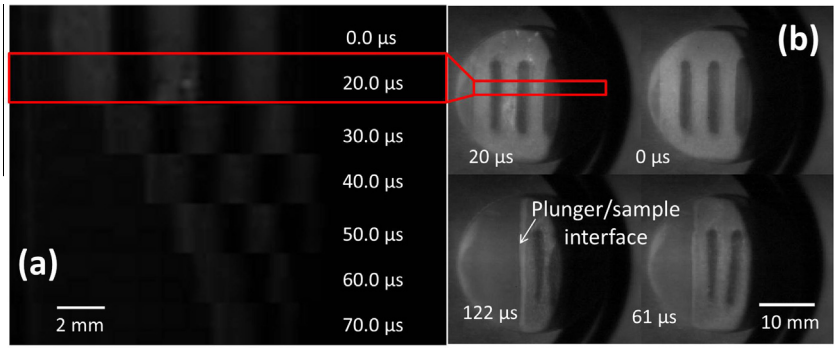

Fig. 13. (a) Snapshots showing motion of reference lines (indicated here in black) on specimen surface after impact with plunger. (b) Snapshots of flat plunger impact on specimen at $v_p = 139$ m/s starting at impact with plunger up to 122 μs.

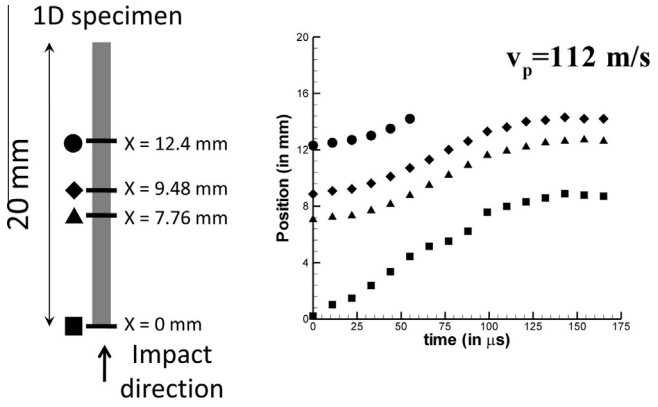

Fig. 14. Experimental observations of material point position in specimen (indicated by schematic on left) as function of time for impact velocity $v_p = 112$ m/s.

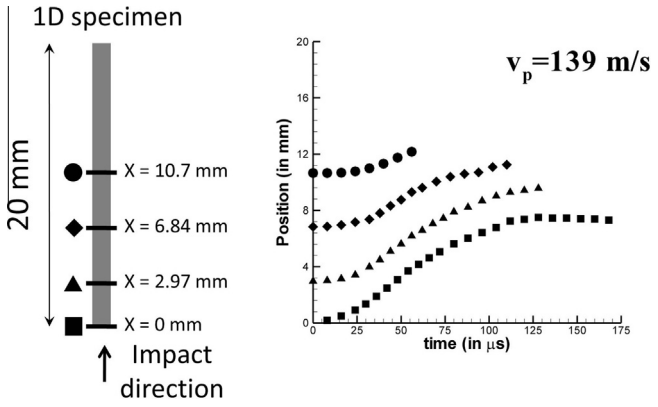

Fig. 15. Experimental observations of material point position in specimen (indicated by schematic on left) as function of time for impact velocity $v_p = 139$ m/s.

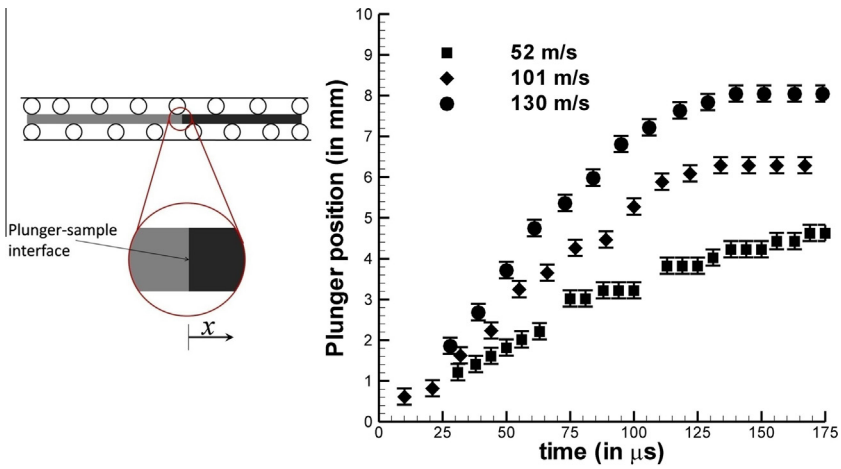

Fig. 16. Experimental observations of plunger-specimen interface displacements for impact velocities $v_p = 52$, 101 and 130 m/s. The uncertainty in displacements are indicated in error bars.

parallel to its impact edge, perpendicular to the impact direction. In the experimental setup, the surface of the specimen containing reference lines is exposed through a circular acrylic window (Fig. 10)) and illuminated by an Xenon-Hg arc lamp.

Table 1
Material Properties of Projectile, Plunger (Marsh, 1980) and Compact specimen (Zhang et al., 2011).

Projectile (Delrin/Steel)		Plunger (Steel)		Specimen (Ni/Al composite)	
ρ_0 (g/cc)	1.932	ρ_0 (g/cc)	7.83	ρ_0 (g/cc)	3.412
ν	0.45	ν	0.33	ν_s	0.34
E (GPa)	21.6	E (GPa)	217	E_{Ni} (GPa)	221
		Γ_0	2.17	E_{Al} (GPa)	70
		s	1.49	m_{Ni}/m_{Al} (%)	30/70
				Q (GPa)	47.27
				q	8.09
				Y_{Ni} (MPa)	380
				Y_{Al} (MPa)	276
				$c_{p,Ni}$ (J/kg-K)	444
				$c_{p,Al}$ (J/kg-K)	897
				$\varphi_0(\%)$	30

High speed cameras (Phanotom v7.3, and Photron FASTCAM SA4) record the movement of the reference lines during the impact event that can be used to construct the trajectory of individual material points during deformation. Shown in Fig. 13 are snapshots of the plunger impacting the powder compact and movement of the reference lines during the transient response of the system. As shown in the Fig. 13(a), the motion of individual lines can be used to construct a picture of material deformation at each demarcated zone on the specimen. Figs. 14 and 15 are the deformed positions of discrete points identified on the surface of the specimen (indicated by the schematic on the left) at impact velocities (v_p) of 112 and 139 m/s, respectively. These data were captured using high speed cameras operating at capture rates of up to 500,000 fps (frames per second). Additionally, the plunger-specimen interface was also tracked for several micro-seconds of specimen deformation after impact. Fig. 16 is a compilation of the plunger-specimen interface displacements for three projectile impact velocities of 52, 101 and 130 m/s. The experimental observations are however prone to uncertainties in displacements due to the capture frame rates of the recording equipment (uncertainty in time; i.e. the time at which the plunger comes into contact with the specimen) and pixel resolution (position uncertainty; i.e. the size of each pixel). The uncertainty in time was resolved by iteratively shifting the data points along the time (horizontal) axis until a segmented fit of the linear portion of the plunger-displacement curve for each impact velocity passes through the origin of the axis. Also indicated in Fig. 16 is the uncertainty in the position of the interface for each instance of impact velocity. The uncertainty on the positions in Fig. 14 and 15 were ±0.13 mm, but are not included in the figure.

From a wide set of impact experiments on the Ni/Al reactive composite the threshold velocity (i.e., the minimum impact velocity to initiate a chemical reaction in the specimen) was determined to be 90 m/s.[8] At impact speeds just above the threshold velocity, it was observed that the reactions in the specimen were delayed (on the order of several milli-seconds). Since we focus entirely on the time-scale of mechanical equilibration of the system (in the order of micro-seconds), we can preclude the effect (s) of mechano-chemical coupling and verify the continuum models proposed in this paper using experimental results of mechanical response of the system before chemistry is initiated (i.e. during pressurization of the system). As a first order approximation we assume that (a) all material deformations are constrained to a single dimension, along the axial direction of the specimen (in the direction of impact; hence we can only compare against results from gas-gun experiments with flat plunger), (b) an uniform distribution of porosity in the system, and (c) contact areas for the three bodies are the same. While the last assumption is true for the plunger and specimen it should be noted that the projectile is in reality a large cylindrical, hollow shell of Delrin with a cap of steel at its impact end with the steel plunger (see Fig. 10). Hence, it is non-trivial to accommodate all the details of the projectile geometry in one-dimensional modeling. We further ignore all plastic deformations that may occur in the projectile and plunger during the impact event.[9] Specifically, the projectile is modeled as a perfectly elastic isotropic material, while the steel plunger is modeled with a Mie–Gruneisen shock EOS with no underlying model for plasticity. The material properties of the projectile, plunger and compact specimen are listed in Table 1.

The material hardening parameters for the J_2 model are, $1/n = 0.1, 1/m = 0.005, \dot{\epsilon}_0^p = 1$. The material properties for the compact specimen were calculated through non-linear curve fitting of parameteric values for elemental Nickel (Ni) and Aluminum (Al) obtained from Zhang et al. (2011) (see Eqs. 8 and 9). The value of composite properties of the matrix material such as Young's modulus (in both projectile and compact specimen) and yield strength (Y) are calculated through a simple rule-of-mixtures based on the mass fractions of the constituent materials. Shown in Fig. 17, is the variation of the α parameter as a function of pressure (see, Eq. 26) for the material properties given in Table 1. The value of macroscopic yield strength (σ_0) of the compact specimen was estimated through the procedure described in Section 4.2.

[8] Threshold velocity is a function of material pre-processing and particle size (Reeves et al., 2010).
[9] This assumption was generally true for impact speeds less than 150 m/s.

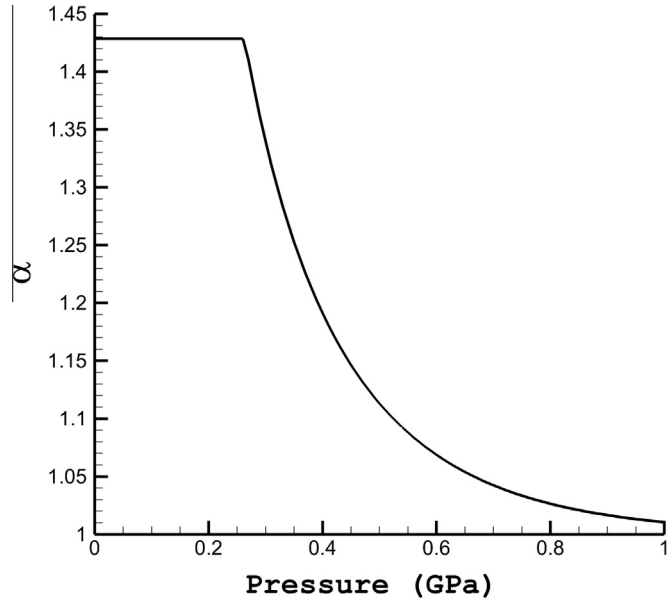

Fig. 17. Plot of inverse solid volume fraction (α) as a function of pressure (p) (Eq. 26) for the material properties given in Table 1.

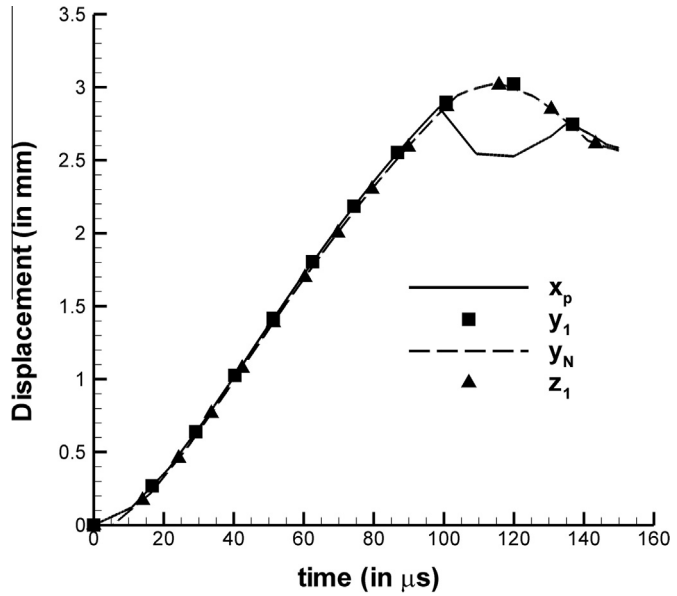

Fig. 18. Time history of contact pair displacements at interface of plunger-projectile (x_p, y_1) and plunger-specimen (y_N, z_1) at v_p=52 m/s.

4.1. Contact implementation

The energy and momentum transfer between the bodies during the impact event, are simulated through one-dimensional (1D) contact modeling. In this section we verify the implementation of the 1D contact model for a projectile impact velocity (v_p) of 52 m/s and the specimen with the proposed continuum model (see, Section 3.3.1). The classical penalty formulation is used to enforce contact conditions between the various interacting pairs in the simulation. In Fig. 11, relevant contact pairs in the 1D model are identified for clarity namely, (x_p, y_1) and (y_N, z_1). In the discretized 1D system x_p is current coordinate of the last node of the projectile, y_1 is the current location of the first node on the plunger similarly, y_N is the last node of the plunger, while z_1 is the first node of the specimen. For the enforcement of displacement continuities at material interfaces, a

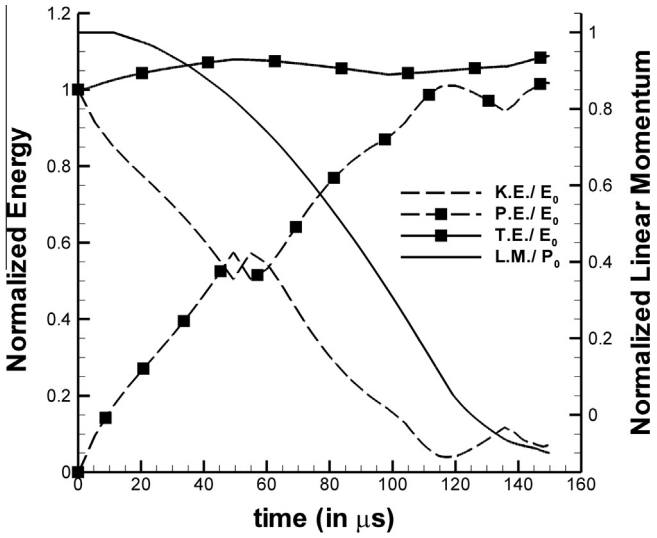

Fig. 19. Time history of normalized energies (total energy (T.E.), kinetic energy (K.E.) and potential energy (P.E.)) and linear momentum (L.M.) of the system at v_p=52 m/s. The energy of the system is normalized with $E_0 = \frac{1}{2} m_p v_p^2$ (Input Energy), while momentum is normalized against $P_0 = m_p v_p$ (Initial Momentum of the system).

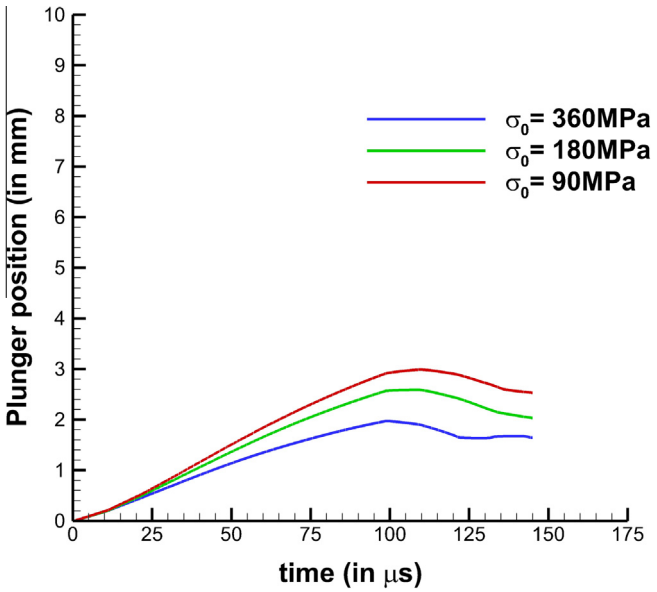

Fig. 20. Effect of increasing macroscopic yield stress, σ_0 on plunger displacement predictions at v_p= 130 m/s.

penalty force is added to the relevant contact pairs at every time-step. In this particular implementation of the penalty method, the magnitude of force on the contact pairs $f^c(x_p, y_1)$ and $f^c(y_N, z_1)$ are,

$$f^c(x_p, y_1) = K_1(x_p - y_1) \text{ iff } x_p > y_1, \quad f^c(y_N, z_1) = K_2(y_N - z_1) \text{ iff } y_N > z_1,$$

In these simulations, the values of contact stiffness K_1 and K_2 are chosen to be 10^{16} and 10^{14} N/m^3, respectively. The undeformed lengths of the projectile (L_0^{proj}), plunger (L_0^{pl}) and specimen (L_0^{sp}) are, 0.32 m, 0.0315 m and 0.02 m, respectively. The contact areas of the materials are assumed to be the same, $A_0 = 4 \times 10^{-5}$ m^2. As can be seen in Fig. 18 the penalty method enforces the displacement continuity at material interfaces quite well. Fig. 19 is a time-history of energy and linear

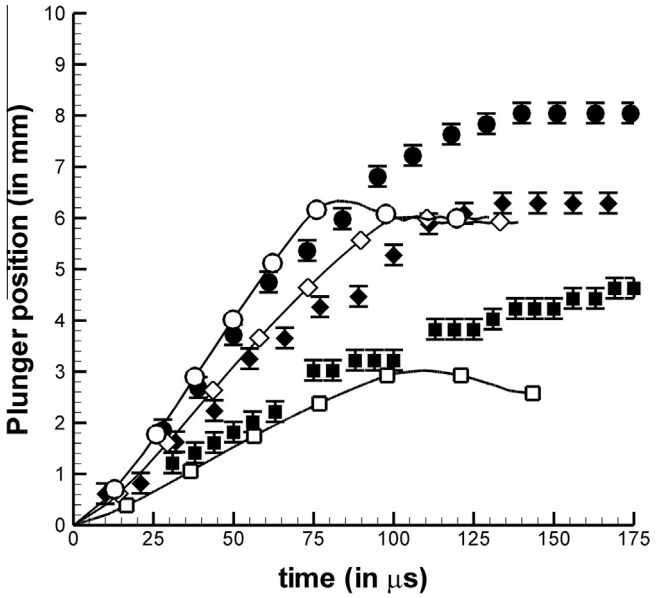

Fig. 21. Comparison of displacements at plunger-specimen interface using proposed continuum model (open symbols). The symbols correspond to v_p= 52 (□), 101 (◇) and 130 m/s (○).

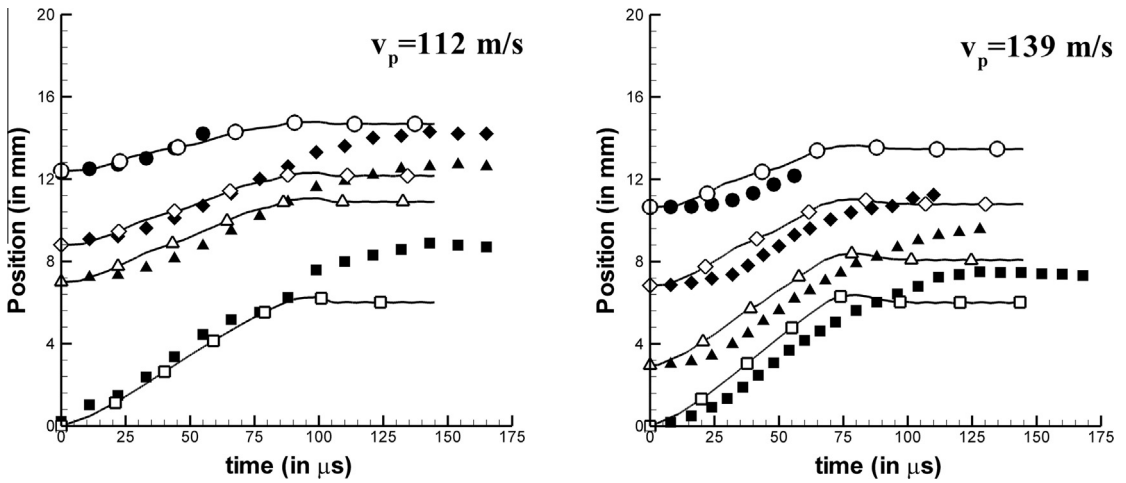

Fig. 22. Numerical prediction of material point position in specimen as function of time (open symbols) for impact velocity $v_p = 112$ m/s (on left) and $v_p = 139$ m/s (on right).

momenta normalized against the input energy[10] and initial momentum[11] of the system, respectively. For a 1D problem, we can define the following quantities,

$$\text{P.E.} = \int_t \int_{L_0} \mathbf{P} : \dot{\mathbf{F}} d\tau dX, \tag{60}$$

$$\text{K.E.} = \int_{L_0} \frac{1}{2} \rho_0 v^2 dX, \tag{61}$$

$$\text{L.M.} = \int_{L_0} \rho_0 v dX, \tag{62}$$

[10] Input energy, $E_0 = m_p v_p^2/2$, where m_p is mass per unit area of projectile and v_p is the initial velocity of the projectile.
[11] Initial linear momentum, $P_0 = m_p v_p$.

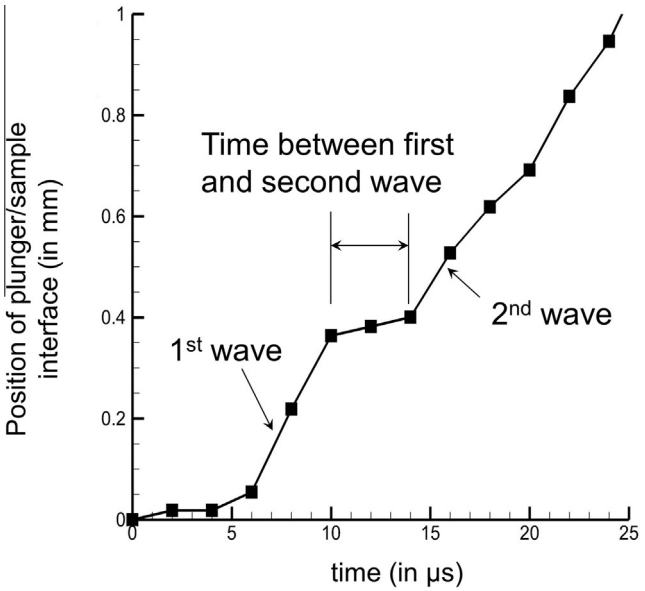

Fig. 23. Identification of primary and secondary waves from impact experiments on Ni/Al powder compact specimen by tracking material point positions at plunger/sample interface at $v_p = 139$ m/s.

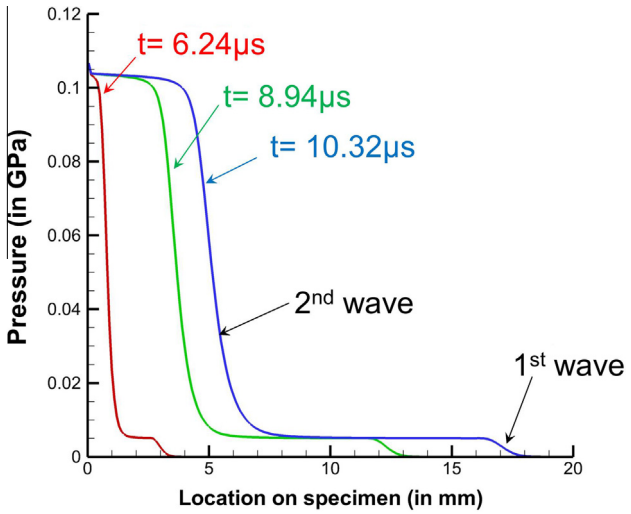

Fig. 24. 1D simulation predictions of wave position in specimen at various times after impact with plunger (for $v_p = 139$ m/s).

where, P.E. is the potential (strain) energy per unit area, K.E. is the kinetic energy per unit area while L.M. is the linear momentum per unit area of the entire system. The quantity 'L_0' designates the domain of integration over the undeformed length (s) of the system (i.e., $L_0 = L_0^{\text{proj}} + L_0^{\text{pl}} + L_0^{\text{sp}}$). Clearly, we see that the total energy (T.E.) of the system is preserved while the total momentum of the system rapidly degrades as the system comes to rest at the end of impact event. The slight increase in T.E. can be attributed to the contact formulation (Gonzalez et al., 2010).

4.2. Prediction of mechanistic response to impact

The yield parameter (σ_0) is necessary for constitutive model calculations of plasticity at the macroscopic level. While the parameter is a function of specimen porosity, in this work the value of macroscopic yield stress for the compact Ni/Al specimen (of 70% initial TMD) was determined by matching plunger displacement predictions at $v_p = 52$ m/s to experimental data. Numerical predictions of plunger displacements at $v_p = 52$ m/s with σ_0 = 90 MPa was seen to agree well with observations from gas-gun experiments at $v_p = 52$ m/s. Since the initial TMD of all compact specimens were approximately 70%,

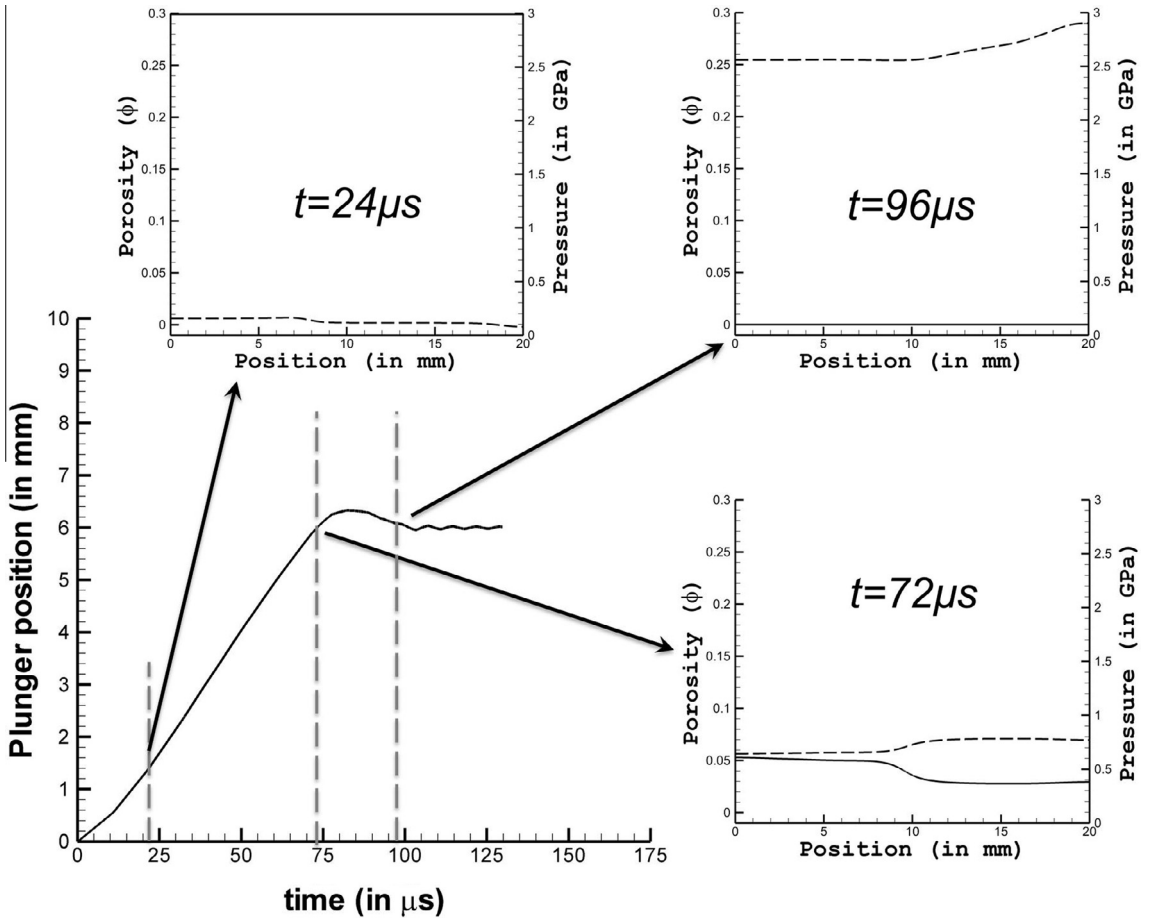

Fig. 25. Predictions of porosity (solid line) and pressure (dashed line) in compact specimen at t = 24, 72 and 96 μs after impact with plunger, for a projectile impact speed, $v_p = 130$ m/s.

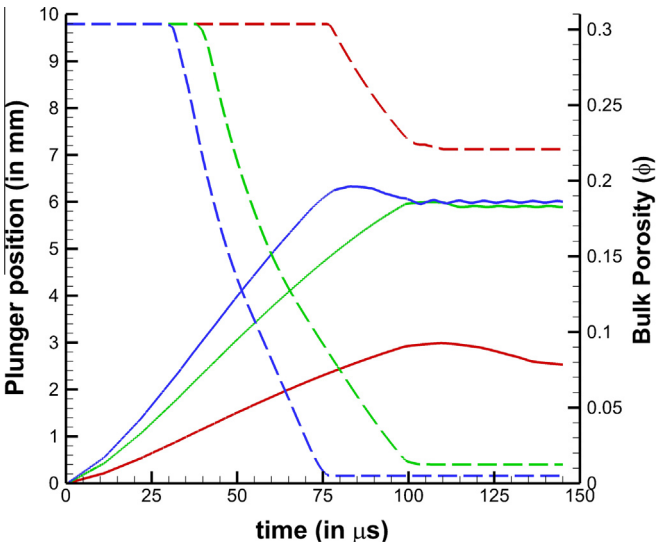

Fig. 26. Predictions of average (or bulk) porosity (φ, dashed line) of the specimen as a function of time and bulk compression (given by plunger position y_N, solid line). The colors represent impact velocities, $v_p =$ of 52 (red), 101 (green) and 130 m/s (blue). (For interpretation of the references to colour in this figure caption, the reader is referred to the web version of this article.)

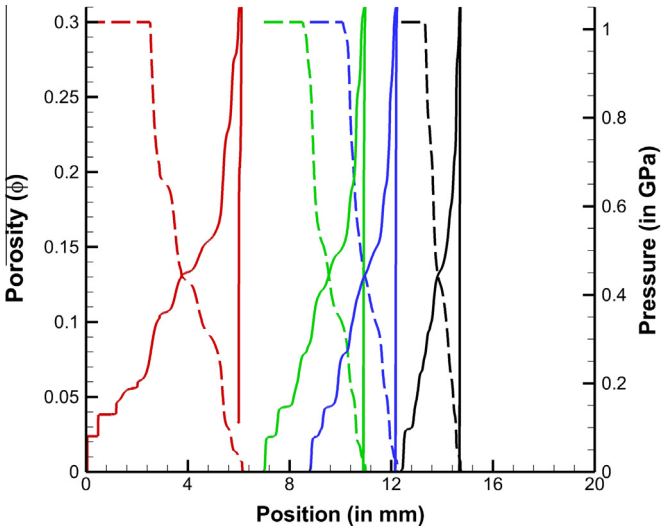

Fig. 27. Evolution of local porosity (dashed line) and pressure (solid line) at material point initially located at $X_0 = 0$ mm (red), 7 mm (green), 8.8 mm (blue) and 12.4 mm (black) as a function of current coordinates when sample is subject to $v_p = 112$ m/s. (For interpretation of the references to colour in this figure caption, the reader is referred to the web version of this article.)

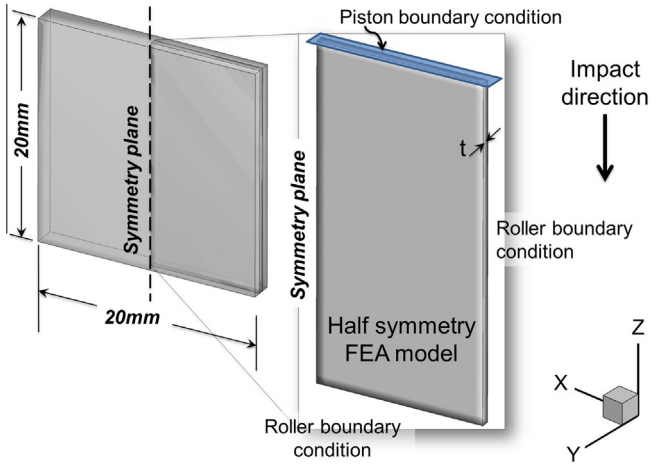

Fig. 28. Setup of three-dimensional model with piston boundary condition. Model symmetry and the relevant boundary conditions are indicated. Thickness (t) of quasi 3D model was chosen to be 0.2 mm.

this value of σ_0 was used for all subsequent predictions. Shown in Fig. 20, are predictions of bulk compression behavior of the specimen at $v_p = 52$ m/s as a function of varying σ_0. We see that the slope of the curves (which is the instantaneous plunger velocity) decreases significantly when the macroscopic yield parameter, σ_0 is increased. A higher yield stress results in a delayed macroscopic yielding of the compact which in turn elicits a softer (viz. a lower slope on the plunger displacement versus time curve) material response. The plunger stoppage position (i.e. the maximum compaction of the specimen at a given impact velocity) on the other hand, occurs when the material is pressurized enough through bulk compression to resist any further deformation. Higher yield values implies lower pressures (hence smaller changes in volume) are required to stop the plunger from moving into the material, thus we see that the plunger stoppage positions decrease as the yield value is increased.

Fig. 21 shows predictions of plunger displacement (from 1D simulations) as a function of time for projectile velocities of 52, 101 and 130 m/s compared to experimental results. Fig. 22 compares the simulation predictions for material point positions within the specimen body as a function of time to results of gas-gun experiments. This comparison provides a rigorous validation of the proposed constitutive model since it tracks the mechanistic response of the material as it spans multiple reflections of the pressure (shock) wave during its transient response. To the knowledge of these authors, this level of exper-

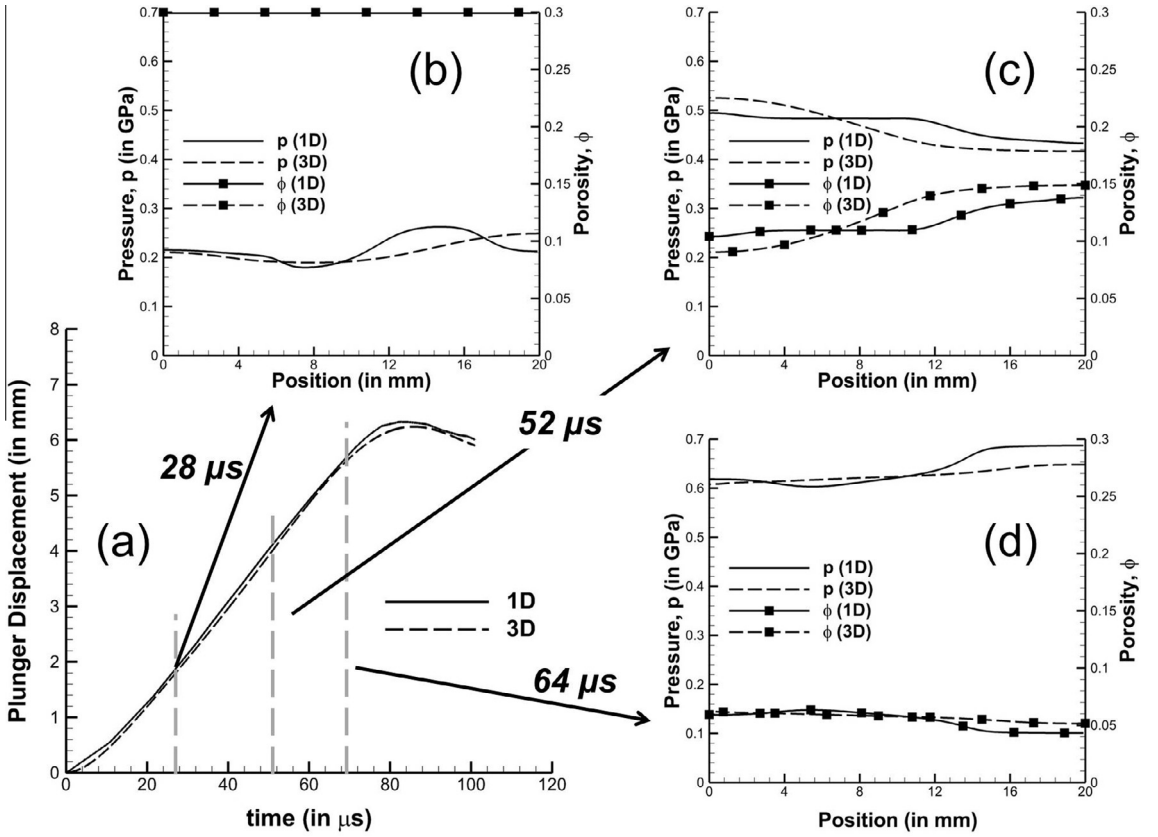

Fig. 29. Comparisons of (a) Plunger displacement curve from one-dimensional (1D) simulation and the corresponding polynomial curve-fit of plunger displacement that was input into three-dimensional (3D) simulation (shown here in dashed line). Pressure (no symbol) and porosity (with symbol) distribution from 1D (solid line) and 3D (dashed line) simulations at (b) t = 28μs, (c) 52 μs, and (d) 64 μs.

imental validation of predictive models for energetic materials subjected to threshold impact velocities in a continuum setting has never been attempted before.

The propagation of stress waves in the sample subject to dynamic compaction is an area of active research. As mentioned in the literature review (in Section 1), moderate input energies can force a stress bridging behavior within powder compacts that results in a clearly defined two wave structure propagating through the powder bed (Menikoff, 2001). However, the onset of the said "stress bridging" is a function of the mechanical properties of the particles that constitute the powder compact. At the threshold impact velocities considered in this work, a distinct and discernible primary wave was observed to propagate through the Ni/Al powder compact for all impact velocities, however, the occurrence of a clearly defined secondary wave in the material was rare for most cases of impact. Fig. 23 is one example of a two-wave structure that could be identified in the material after impact with plunger at $v_p = 139$ m/s. The wave speed (s) can be computed by tracking the time at which there is a noticeable change in slope of the material position versus time curves (i.e., Figs. 14 and 15) for each material point location. In this particular case of impact, the velocity of the 1st and 2nd waves were determined to be 2.7 km/s and 0.46 km/s, respectively. The 1D simulations in this work predicts a clearly defined two wave structure, as seen in Fig. 24. The instantaneous position of the waves can be used to determine the wave velocities in the material. In these simulations the wave velocities were determined to be 3.46 km/s and 1.06 km/s. While the model predictions for wave velocities are fairly close, we do not draw any particular conclusions from these results, however it is shown that gas-gun experiments are a viable method to characterize dynamic behavior of powder compacts and warrants further investigation.

The proposed material model also solves for porosity in the material as part of the constitutive update (as described in Section 3.3.1). Fig. 25 shows predictions of pressure and porosity distribution inside the material at various times, due to the action of the plunger (which has been impacted with a projectile velocity, v_p=130 m/s) on the specimen. For an impact velocity of 130 m/s, 1D simulations predict that there is a complete collapse of the pores in the material at the end of 90 μs. Fig. 26 shows predictions of bulk compaction (indicated by decrease in volume averaged porosity) of the specimen due plunger impact. Fig. 27 is the evolution of local porosity and pressure in the specimen subject to projectile impact speed of 112 m/s. It is clearly evident from these predictions that as the material is subjected to increasingly higher impact velocities (hence higher input energies), higher internal pressures develop in the specimen (due to larger volume deformations) that results in a greater consolidation of the material. The results underscore the influence of local pressure on the pore collapse

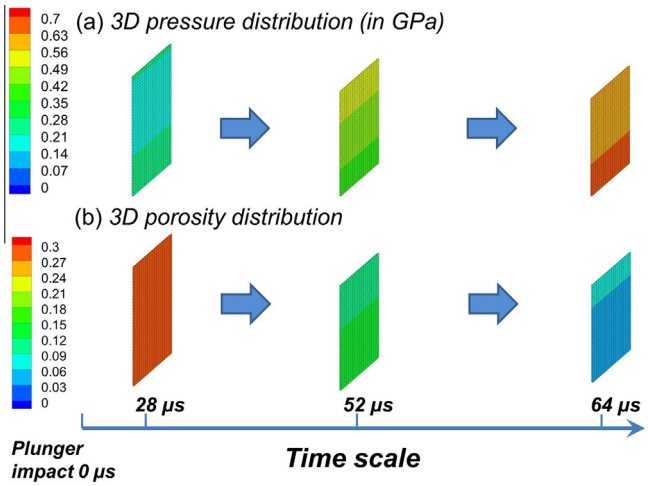

Fig. 30. Distributions of (a) Pressure and (b) Porosity from 3D flat plunger impact simulations. Mesh deformation is also depicted in these time-snapshots.

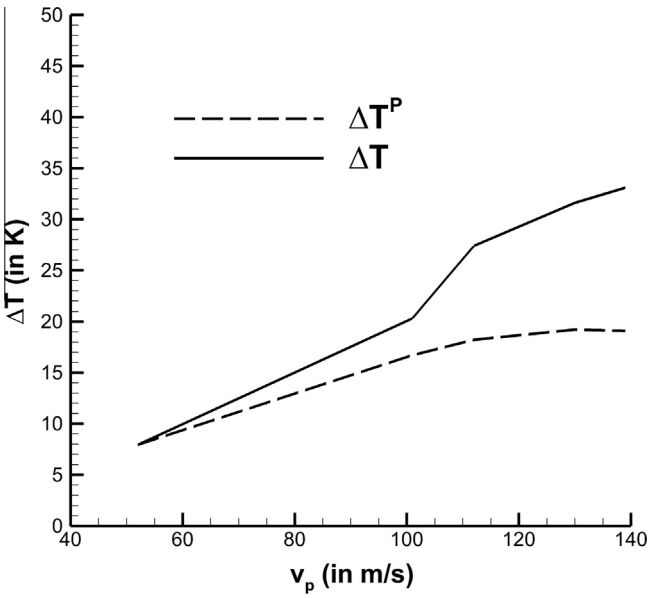

Fig. 31. Prediction of average total temperature (ΔT) and plastic temperature (ΔT^{P}) increases in a 70% TMD (30% porosity) Ni/Al composite as a function impact velocity, v_p.

inside the material. In general, it is seen that 1D simulations with the proposed constitutive model renders a stiffer response in its predictions especially at higher impact velocities (i.e., for $v_p > 100$ m/s). It is hypothesized that the stiffer response can be directly attributed to the 1D constraints placed on material deformation. A detailed discussion on the constraints is provided in Section 5.2.

In order to demonstrate and validate the proposed constitutive approach in a three-dimensional (3D) setting, the impact of flat plunger that is subject to projectile impact at 130 m/s on a quasi-3D model was studied. Fig. 28 is a schematic of the 3D-FEA model geometry along with boundary conditions. Plane strain conditions were adopted on the specimen geometry such that it does not deform in the out of plane (along Y-axis) direction. The thickness of the simulation model was chosen to be 0.2 mm (1/10th the actual thickness of the specimen). The plunger impact on the specimen was simulated by moving nodes at the top surface (i.e. the Z = 20 mm plane) of the specimen, downward along the negative Z-axis using a piston boundary condition. The velocity profile of the piston was obtained from curve-fitting one-dimensional plunger displacement result with a 6th degree polynomial (see Fig. 29(a)). The specimen was discretized using a $40 \times 1 \times 80$ mesh with six (6) node quadratic tetrahedral elements (19,200 elements in total). The time-step of the integrator was fixed at 10^{-5} μs. Since field variables only vary in the direction normal to the impact plane (i.e., the Z-axis in this simulation) in case

Table 2
Coefficients in Eq. (64).

i	c_i (in MPa)
0	-3.109×10^{11}
1	1.62×10^{12}
2	-3.413×10^{12}
3	3.772×10^{12}
4	-2.32×10^{12}
5	7.55×10^{11}
6	-1.018×10^{11}

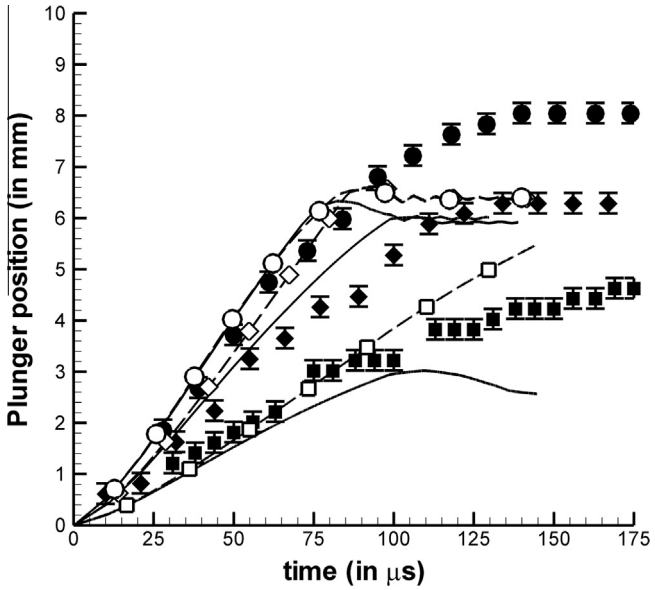

Fig. 32. Results for BCC micromechanical model. Comparison of displacements at plunger-specimen interface in dynamic pore collapse (open symbols). CH model results are indicated by solid lines.The symbols correspond to v_p= 52 m/s (□), 101 m/s (◇) and 130 m/s (○).

of the flat plunger impact, we can directly compare pressure and porosity distributions predicted by 1D and 3D calculations (see, Fig. 29). As evident from Fig. 29(b)–(d), 3D FEA is able to reproduce the 1D simulation results robustly under similar load and boundary conditions. The minor differences in the result can be attributed to (a) the much coarser 3D mesh (the 1D model was divided into 200 segments along its length) and, (b) dissimilar plunger displacements (i.e. the error in curve-fitting). Fig. 30 shows 3D simulation predictions of pressure and porosity distribution in the specimen as it is compacted by the plunger.

4.3. Prediction of material heating due to Impact

An (important) application of the predictive model developed in this paper will be to incorporate chemistry models for reaction initiation and propagation with a mechanics based ignition criterion to simulate (and predict) stress-assisted chemistry in energetic materials. To this end, the effective rise in temperature in the continuum model is computed using Eqs. (13) and (20). For the discussions to follow we define the average temperature rise $\langle \Delta T \rangle$ as,

$$\langle \Delta T \rangle = \frac{\sum_{i=1}^{N} \Delta T_i}{N}, \tag{63}$$

where, $\Delta T_i = \Delta T_i^{\mathrm{P}} + \Delta T_i^{\mathrm{S}}$, is the total temperature rise at a node 'i' and N is the total number of nodes in the discretized 1D model of the specimen. We assume that the temperature in the specimen is raised adiabatically (i.e., with no heat loss to the environment) through plastic dissipation and shock related heating. Given the extremely short time-scale of mechanical equilibration, these assumptions seem quite reasonable. It should also be noted that in the results to follow the heat capacity of the material is estimated through a simple rule of mixtures based off the mass-fraction in the Ni/Al binary composite. While it may not be a realistic description of the thermodynamic property of the composite, it provides as a crude first order

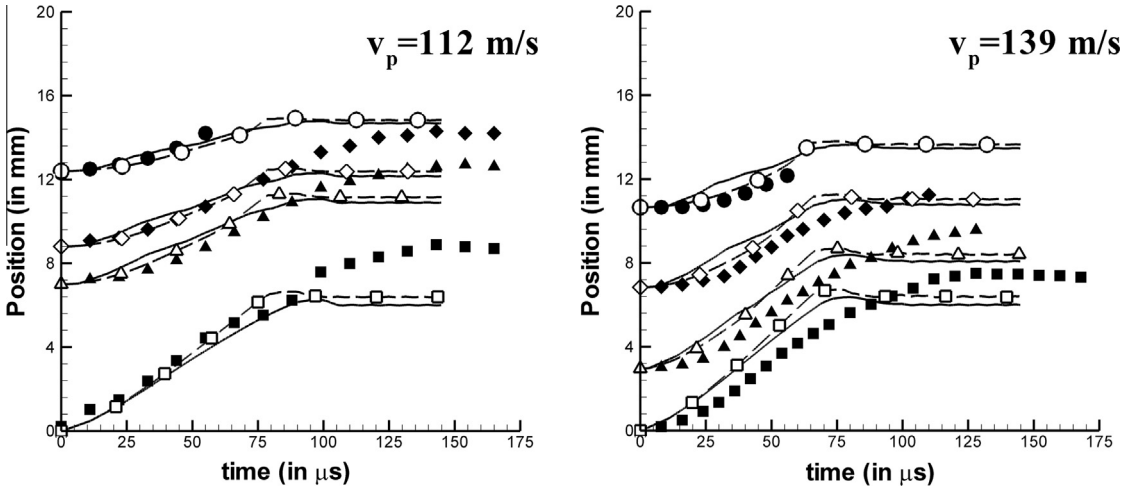

Fig. 33. Results for the BCC micromechanical model. Numerical prediction of material point position in specimen as function of time (open symbols) for impact velocity $v_p = 112$ m/s (on left) and $v_p = 139$ m/s (on right). CH model results are indicated by dashed lines.

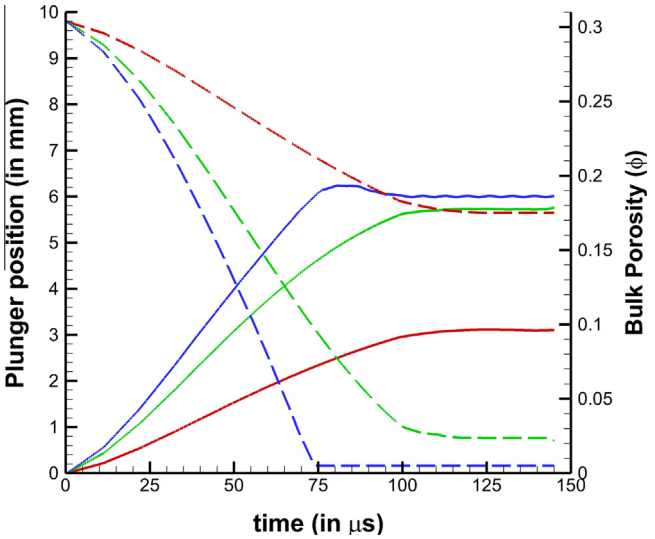

Fig. 34. Predictions of average (or bulk) porosity (dashed line) of the specimen as a function of time and bulk compression (solid line) for the BCC micromechanical model. The colors represent impact velocities, $v_p =$ of 52 (red), 101 (green) and 130 m/s (blue). (For interpretation of the references to colour in this figure caption, the reader is referred to the web version of this article.)

estimate of the temperature increase in the specimen during the impact simulation. Shown in Fig. 31 is the average temperature rise in the material (computed in Eq. 63) as a function of impact velocity on a 70% TMD material with uniform (i.e., spatially invariant) distribution of porosity. Also included in the figure is the contribution of plastic dissipation (ΔT^{P}) to ΔT, the shock assisted heating (ΔT^{S}) is the difference between the two plots. Clearly, plastic deformation of the material plays a significant role in material heating at lower to threshold impact velocities. As impact velocities increase, the increasing shock energy dominates the "heat-up" of the specimen. These numerical observations are consistent with prior experimental work on Ni/Al powders (Thadhani, 1994).

Since, the material constitutive model explicitly accounts for pore collapse in the material along with its related effects on heating the material during the course of deformation, it is envisioned that the proposed simulations scheme can be effectively used to capture many of the microscale localization mechanisms inherent to porous materials in a continuum setting without resorting to a full-scale discrete particle mechanics algorithm. It is expected that by switching to 3D-FEA simulations, additional effects of frictional heating due to contact with external bodies (viz., the plunger/specimen interface or

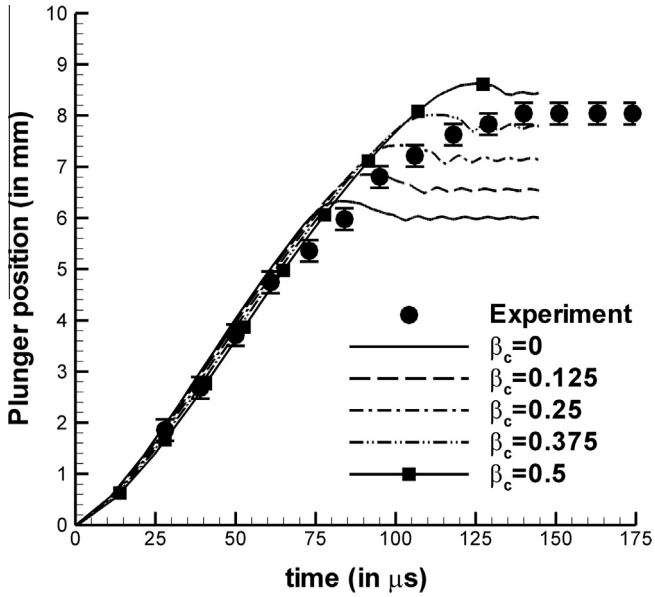

Fig. 35. Effect of relaxing 1D constraint on predictions of plunger displacement using the CH model analysis at impact velocity $v_p = 130$ m/s. Experimental results are indicated in symbols.

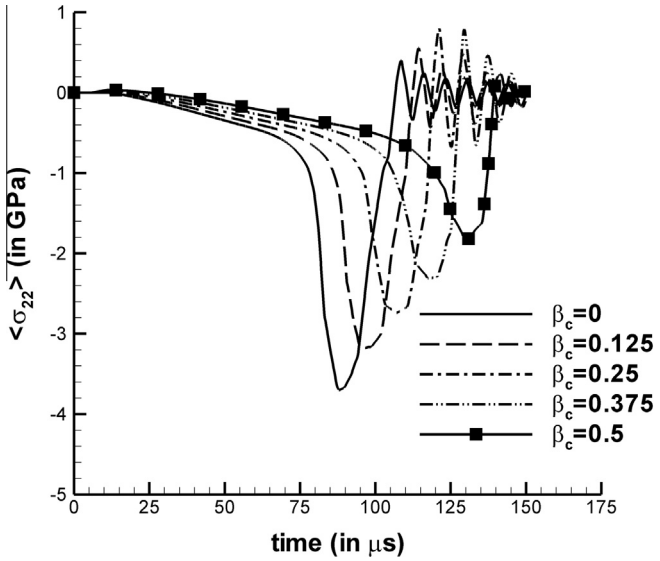

Fig. 36. Effect of relaxing 1D constraint on average constraint stress σ_{22} in static pore collapse analysis at impact velocity $v_p = 130$ m/s.

specimen/boundary wall interaction) can be incorporated into the simulation. In this manner, the proposed simulations technique will be able to supplement chemistry models in the prediction of initiation and progression of reactions in energetic materials.

5. Discussion

From the results discussed in Section 4 we clearly see that the proposed model is a viable tool to simulate the mechanistic response of porous, heterogenous energetic materials. In this section, we delineate the effect of microstructure (Section 5.1 and 1D constraints (Section 5.2) on the overall material response predictions. By studying these effects, we will be able to achieve a better understanding of the proposed constitutive model.

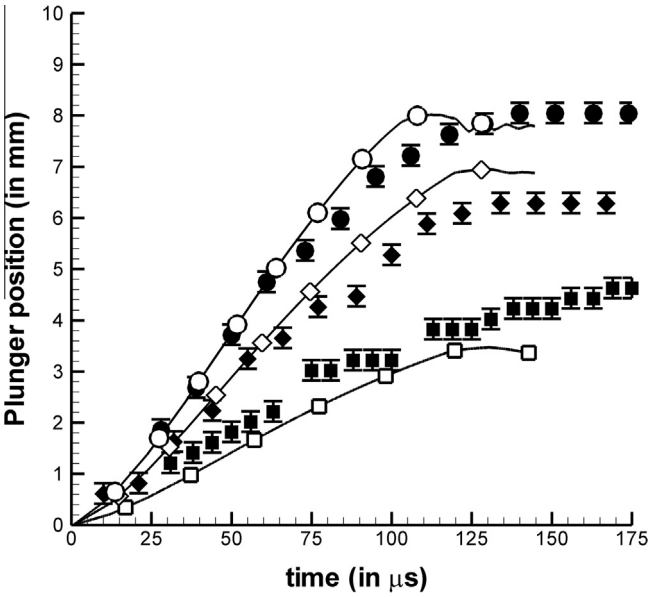

Fig. 37. Comparison of displacements at plunger-specimen interface using the CH model, with relaxed 1D constraints ($\beta_c = 0.375$). The symbols correspond to v_p= 52 (□), 101 (◇) and 130 m/s (○).

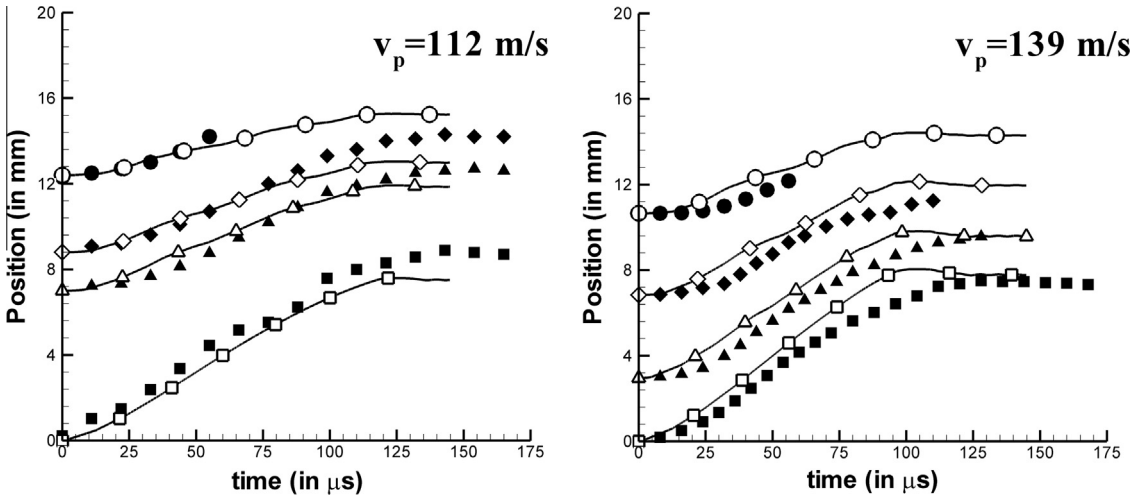

Fig. 38. Numerical prediction of material point position in specimen as function of time (open symbols) for impact velocity $v_p = 112$ m/s (on left) and $v_p = 139$ m/s (on right) using CH model, with relaxed 1D constraints ($\beta_c = 0.375$).

5.1. Effect of microstructure

In Section 2.3.2, an alternate approach to RVE modeling of porous materials was suggested. To this end, Eq. (31) was parametrized by curve-fitting to the hardening law in Eq. (33). In this case, the curve fit parameters were determined to be $\kappa = 530$ MPa and $m \approx 3$. Following this, quasi-static (excluding dynamic effects) particle level simulations of hydrostatic compression of the BCC packing (depicted in Fig. 7), were used to determine the pressure developed in the model (p) as a function of α by post-processing the simulation results. A 6th order polynomial fit (Eq. 64) was used to describe '$p(\alpha)$'. The coefficients of the curve-fit are listed in Table 2.

$$p(\alpha) = \sum_{i=0}^{6} c_i \alpha^i. \tag{64}$$

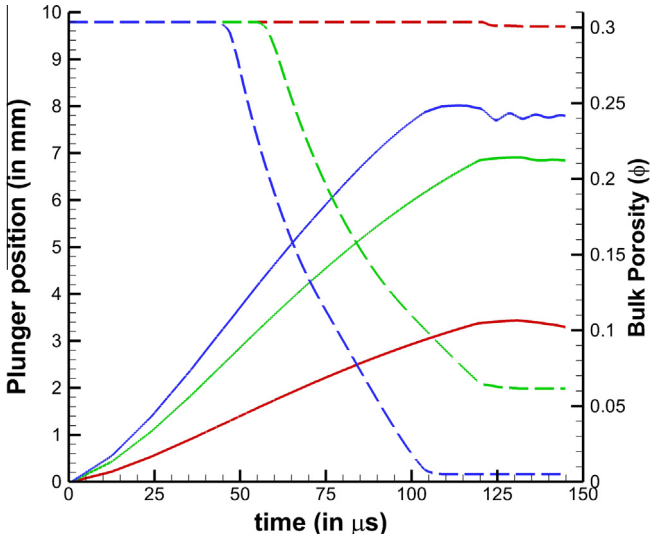

Fig. 39. Predictions of average (or bulk) porosity (dashed line) of the specimen as a function of time and bulk compression (solid line), with relaxed 1D constraints ($\beta_c = 0.375$). The colors represent impact velocities, $v_p =$ of 52 (red), 101 (green) and 130 m/s (blue). (For interpretation of the references to colour in this figure caption, the reader is referred to the web version of this article.)

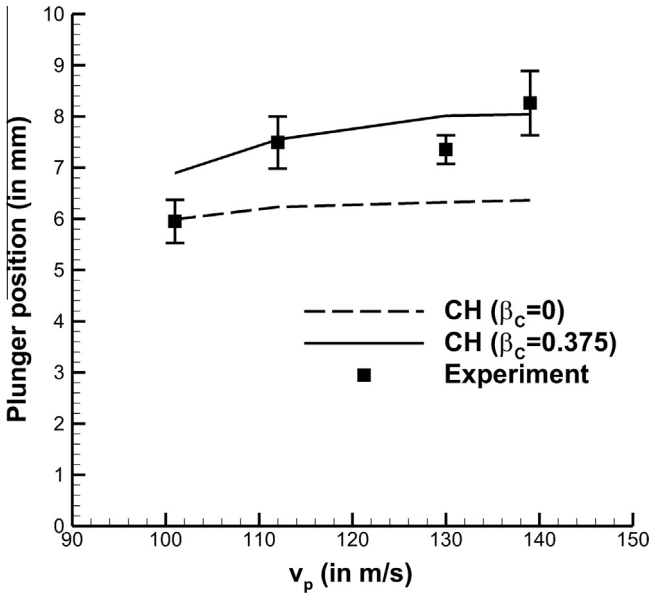

Fig. 40. Comparison of predictions of plunger positions (or maximum compression of specimen) between CH model with $\beta_c = 0$, CH model with relaxed lateral constraints ($\beta_c = 0.375$) and experimental observations (with standard deviation of results indicated by error bars) as a function of impact speed, v_p.

The results from the particle-mechanics simulations were incorporated into the continuum model. The equation of state pressure was computed using Eq. (64) whenever, $\alpha > 1$, and Eq. (12) when $\alpha = 1$ (after full void collapse). The macroscopic yield parameter of σ_0=90 MPa was used in these simulations. For the sake of clarity and convenience, we will denote the RVE model for void collapse given in Section 2.3 as CH, while the model proposed in Section 2.3.2 as BCC. Fig. 32 is time-history of plunger displacement for various projectile velocities, while Fig. 33 show predictions of material point position within the specimen body as a function of time. Results from simulation with CH model are included in the above plots for comparison. Fig. 34 shows the multi-scale, micromechanical model predictions for bulk porosity as a function of compaction at various impact speeds. It is evident that at lower impact velocities the micro-structural description influences the pore collapse behavior. A key reason for this difference is the fact that in the CH model (Section 2.3) the pore-collapse within the material is delayed until $p > p_{\text{crit}}$, while the BCC model on the other hand (Section 2.3.2), predicts a continuous decrease of porosity

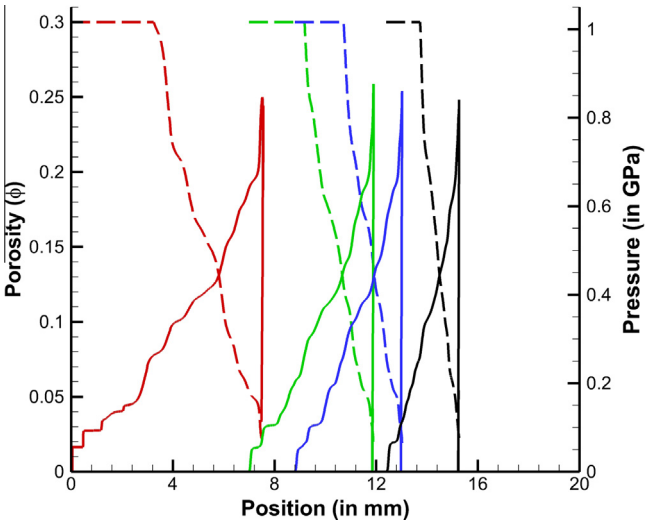

Fig. 41. Evolution of local porosity (dashed line) and pressure (solid line) at material point initially located at $X_0 = 0$ mm (red), 7 mm (green), 8.8 mm (blue) and 12.4 mm (black) as a function of current coordinates when sample is subject to $v_p = 112$ m/s, with relaxed 1D constraints ($\beta_c = 0.375$). (For interpretation of the references to colour in this figure caption, the reader is referred to the web version of this article.)

with all levels of deformation. Hence, specific changes in the description of the micro-scopic RVE directly influences the macroscopic predictions. However it should be noted that as in the case of the CH model, the results are affected by the constraints on the system, which ultimately results in the complete compaction of the material at an impact speed of 130 m/s.

It is the view of these authors that the continuum modeling strategy developed in this work is amenable to multi-scale modeling of energetic materials wherein results of simulation from detailed, large-scale, highly resolved particle-level simulations can be hierarchically incorporated into a macroscopic simulations setting.

5.2. Effect of 1D constraint

As observed from results in the previous sections, the constraints imposed on the solution by 1D assumption tends to restrict material deformation (see, e.g. Figs. 21 and 33, etc.). Furthermore, there is experimental evidence of material expansion in the lateral direction during the course of the impact event. In this section, we try to underscore the effect of relaxing 1D constraints on the overall response of the material system. In a 1D system, the discrete deformation gradient at the beginning of time-step 't_n' for node 'i' can be written as,

$$\mathbf{F}_n^i = \mathbf{F}(X^i, t_n) = \begin{bmatrix} 1+\Delta_n^i & 0 & 0 \\ 0 & 1-\beta_c\Delta_n^i & 0 \\ 0 & 0 & 1 \end{bmatrix}, \tag{65}$$

where, $\Delta_n^i = \frac{x_n^{i+1} - x_n^i - L_0^i}{L_0^i} = \frac{u_n^{i+1} - u_n^i}{X^{i+1} - X^i}$, is a measure of deformation of line segment 'i' of initial (undeformed) length L_0^i with, $x_n^i (= X^i + u_n^i)$ is the current coordinate of node 'i', such that $x_0^i = X^i$ and u_n^i is the displacement of node 'i'. Furthermore, β_c is a constraint parameter included in the deformation gradient such that $\beta_c = 0$ will result in strict 1D constraints, while $\beta_c > 0$ will relax 1D constraints by allowing for lateral expansion as a function of axial strain (Δ_n^i). Shown in Fig. 35 is the effect of increasing the value of β_c (i.e., decreasing the lateral constraint) from 0 to 0.5 on the displacement predictions at $v_p = 130$ m/s. The CH pore collapse model were used in these simulations. Fig. 36 is the plot of average Cauchy stress σ_{22} for each case of 'β_c' at $v_p = 130$ m/s. Figs. 37 and 38 are the displacement predictions from 1D simulations with the CH model, with $\beta_c = 0.375$. Clearly, as the model allows for more lateral expansion and relaxes the constraint stress σ_{22}, the simulation results seem to approach the results from impact tests. As shown in Fig. 39, relaxed boundary conditions has an immediate effect on the final compacted state of the material. Fig. 40 is a comparison of maximum specimen compression predictions from CH model (Section 2.3, with $\beta_c = 0$), and the CH model with relaxed constraints($\beta_c = 0.375$). Also included in the plot are the corresponding experimental observations along with the standard deviation associated with each observation. It is observed that relaxed constraints lowers the maximum pressure in the specimen during the course of the impact simulation at v_p = 112 m/s (see, Figs. 27 and 41) which results in an in-complete compaction of the specimen. These observations seem to suggest that full 3D simulation might realistically model the constraints on the actual specimen at higher impact velocities.

6. Conclusion

In this paper, a macroscopic simulation scheme to model porous energetic materials has been proposed. The constitutive model for the material includes an equation of state for porous solids that describes the evolution of porosity in the material as a function of shock pressure and, a visco-plasticity model that accounts for the deviatoric strength of the material at weak to moderate shock strengths. Results from 1D modeling predictions were rigorously validated against gas-gun assisted impact experiments on Ni/Al IRC at 70% TMD. Modeling predictions at lower impact velocities seemed to be influenced by the RVE microstructure. The effect of over-constraint due to 1D assumption of deformation on simulation predictions were also demonstrated. It is envisioned that incorporating the proposed continuum model into 3D-FEA will enhance predictive capabilities by relaxing constraints and capturing effect (s) of boundary friction on mechanistic response of the system. Also suggested in this work is a viable model to calculate temperature excursions in the energetic materials due to shock and plastic dissipation. While the temperature predictions seem to qualitatively capture the trends in material heating, further experimental validation is necessary to couple results of mechanistic predictions with appropriate chemistry models to study initiation and propagation mechanisms in energetic materials.

Acknowledgements

The authors would like to acknowledge the efforts of their collaborators Mathew J. Cherukara at Purdue University, West Lafayette, Khachatur Manukyan and Alexander Mukasyan at University of Notre Dame to this work. The authors also would like thank Marcial Gonzalez (Rutgers) for discussions and sharing data on his particle-level simulations. This work was supported by funding from the Defense Threat Reduction Agency (DTRA), Grant No. HDTRA1–10-1–0119 with Dr. Suhithi M. Peiris, program director.

References

Austin, R., McDowell, D.L., 2012. Parameterization of a rate-dependent model of shock-induced plasticity for copper, nickel, and aluminum. Int. J. Plast. 32, 134–154.
Barua, A., Horie, Y., Zhou, M., 2012. Microstructural level response of hmx estane polymer-bonded explosive under effects of transient stress waves. Proc. R. Soc. A 279, 1471–2946.
Benson, D.J., Nesterenko, V.F., Jonsdottir, F., Meyers, M.A., 1997. Quasi static and dynamic regimes of granular material deformation under impulse loading. J. Mech. Phys. Solids 45, 1955–1999.
Brünig, M., Driemeier, L., 2007. Numerical simulation of taylor impact tests. Int. J. Plast. 23, 1979–2003.
Carroll, M.M., Holt, A.C., 1972. Static and dynamic pore collapse relations for ductile porous materials. J. Appl. Phys. 43, 1626–1636.
Cuitiño, A.M., Ortiz, M., 1992. A material-independent method for extending stress update algorithm from small-strain plasticity to finite plasticity with multiplicative kinematics. Eng. Comput. 9 (4), 427–436.
Cuitiño, A.M., Ortiz, M., 1993. Constitutive modeling of $l1_2$ intermetallic crystals. Mater. Sci. Eng. A170, 111–123.
Dai, C., Eakins, D., Thadhani, N.N., 2008. Dynamic densification behavior of nanoiron powders under shoch compression. J. Appl. Phys. 103 (093503).
Dijken, D.K., De Hosson, J.T.M., 1994. Shock wave equation of state of powder material. J. Appl. Phys. 75, 809–813.
Eakins, D., Thadhani, N.N., 2007. Discrete particle simulation of shock wave propagation in a binary ni+al powder mixture. J. Appl. Phys. 101, 043508.
Fredenburg, D., Thadhani, N.N., 2013. On the applicability of the p-α and p-λ models to describe the dynamic compaction response of highly heterogeneous powder mixtures. J. Appl. Phys. 113 (043507).
Germain, P., Lee, E.H., 1973. On shock waves in elastic-plastic solids. J. Mech. Phys. Solids 21, 359–382.
Gonzalez, M., Cuitiño, M.A., 2012. A nonlocal contact formulation for confined granular systems. J. Mech. Phys. Solids 60, 333–350.
Gonzalez, M., Schmidt, B., Ortiz, M., 2010. Energy-stepping integrators in lagrangian mechanics. Int. J. Numer. Methods Eng. 82, 205–241.
Grady, D.E., Winfree, N.A., Kerley, G.I., Wilson, L.T., Kuhns, L.D., 2000. Computational modeling and wave propagation in media with inelastic deforming microstructure. J. Phys. IV France 10 (PR9), 15–20.
Herrmann, W., 1969. Constitutive equations for the dynamic compaction of ductile porous materials. J. Appl. Phys. 40, 2490–2499.
Hill, R., Storakers, B., Zdunek, A.B., 1989. A theoretical study of the brinell hardness test. Proc. R. Soc. London A 423, 301–330.
Kuchnicki, S., Radovitzky, R., Cuitiño, A.M., 2008. An explicit formulation for multiscale modeling of bcc metals. Int. J. Plast. 24 (12), 2173–2191.
Kumar, D.R., Kumar, R.K., Philip, P.K., 1999. Simulation of dynamic compaction of metal powders. J. Appl. Phys. 85, 767–775.
Lew, A., Radovitzky, R., Ortiz, M., 2001. An artificial-viscosity method for the lagrangian analysis of shocks in solids with strength on unstructured, arbitrary-order tetrahedral meshes. J. Comput. Aided Mater. Des. 8, 213–231.
Manukyan, K.V., Mason, B.A., Groven, L.J., Lin, Y.C., Cherukara, M., Son, S.F., Strachan, A., Mukasyan, A.S., 2012. Tailored reactivity of ni+al nanocomposites: microstructural correlations. J. Phys. Chem. C 116, 21038–21207.
Marsh, S.P., 1980. LASL Shock Hugoniot Data. University of California Press, Berkeley, CA.
McQueen, R.G., Marsh, S.E., 1991. Shock waves in condensed media: their properties and the equations of state of materials derived from them. In: Eliezer, S., Ricci, R.A., (Eds.), Proceedings of the International School of Physics "Enrico Ferm", Course 113, pp. 101–215.
Menikoff, R., 2001. Meso-scale simulations of compaction waves in a granular bed. In: Proceedings of the 23rd International Symposium on Shock Waves, Fort Worth, Texas, p. 5016.
Meyers, M.A., 1994. Dynamic Behavior of Materials. John Wiley and Sons, Inc.
Mostert, L.B., Viljoen, H.J., 1999. Comparative study of analytical methods for hugoniot curves of porous materials. J. Appl. Phys. 86, 1245–1254.
Mukasyan, A.S., Khina, B.B., Reeves, R.V., Son, S.F., 2011. Mechanical activation and gasless explosion: nanostructural aspects. Chem. Eng. J. 174, 677–686.
Pandey, A., Khan, A.S., Kim, E.Y., Choi, S.H., Gnäupel-Herold, T., 2013. Experimental and numerical investigations of yield surface, texture, and deformation mechanisms in aa5754 over low to high temperatures and strain rates. Int. J. Plast. 41, 165–188.
Radovitzky, R., Ortiz, M., 1999. Error estimation and adaptive meshing in strongly nonlinear dynamic problems. Comput. Methods Appl. Mech. Eng. 172, 203–240.
Ramakrishnan, N., Arunachalam, V.S., 1990. Effective elastic moduli of porous solids. J. Mater. Sci. 25, 3930–3937.
Reding, D.J., 2009. Shock induced chemical reactions in energetic structural materials. Ph.D. thesis, Georgia Institute of Technology.
Reeves, R.V., Mukasyan, A.S., Son, S.F., 2010. Thermal and impact reaction initiation in ni/al heterogeneous reactive systems. J. Phys. Chem. C 114 (35), 14772–14778.
Shojaei, A., Voyiadjis, G.Z., Tan, P.J., 2013. Viscoplastic constitutive theory for brittle to ductile damage in polycrystalline materials under dynamic loading. Int. J. Plast. 48, 125–151.

Simons, G.A., Legner, H.H., 1982. An analytic model for the shock hugoniot in porous materials. J. Appl. Phys. 53, 943–947.
Thadhani, N.N., 1994. Shock-induced and shock-assisted solid-state chemical reactions in powder mixtures. J. Appl. Phys. 76 (4), 2129–2138.
Tong, W., Ravichandran, G., 1993. Dynamic pore collapse in viscoplastic materials. J. Appl. Phys. 74, 2425–2435.
Vocadlo, L., Poirer, J.P., Price, G.D., 2000. Gruneisen parameters and isothermal equations of state. Am. Mineralog. 85, 390–395.
Wallace, D.C., 1980. Flow process of weak shocks in solids. Phys. Rev. B 22, 1487–1494.
Wu, Q., Jing, F., 1996. Thermodynamic equation of state and application to hugoniot predictions for porous materials. J. Appl. Phys. 80, 4343–4349.
Zhang, X., Qiao, L., Shi, A.S., Zhang, J., Guan, Z.W., 2011. A cold energy mixture theory for the equation of state in solid and porous metal mixtures. J. Appl. Phys. 110 (013506).
Zharkov, V.N., Kalinin, V.A., 1971. Equation of State for Solids at High Pressures and Temperature. Consultant Bureau, New York (Translated from Russian by A. Tybulewich).